MODELING OF SINGLET-DELTA OXYGEN YIELDS IN FLOWING ELECTRIC DISCHARGES

BY

DAVID SHANE STAFFORD

B.S., Louisiana State University, 1999

THESIS

Submitted in partial fulfillment of the requirements
for the degree of Master of Science in Chemical and Biomolecular Engineering
in the Graduate College of the
University of Illinois at Urbana-Champaign, 2004

Urbana, Illinois

ABSTRACT

Chemical oxygen-iodine lasers (COIL) are attractive for diverse industrial applications because COIL's are capable of high efficiency, high power operation, and the 1.315 μm wavelength can be transmitted through fiber optics and couples efficiently with most metals. Conventional COILs are pumped with $O_2(^1\Delta)$ that is generated by reaction of Cl_2 in a basic H_2O_2 solution. Current trends in pumping COILs involve producing the $O_2(^1\Delta)$ in electric discharges, thereby circumventing the hazards, complexity, and weight associated with pumping and storing caustic liquids.

In this work, the scaling of $O_2(^1\Delta)$ yields as a function of specific energy deposition in He/O_2 mixtures in flowing radio frequency (rf) discharges at pressures of a few to 10s of Torr has been computationally investigated using a global plasma kinetics model and an axial one-dimensional model. The $O_2(^1\Delta)$ yield was found to increase nearly linearly with specific energy deposition in O_2 molecules up to a few eV per molecule, with yields peaking at ≈30% at 5-8 eV/molecule. Further increases in specific energy deposition serve only to increase O_2 dissociation and gas heating, thereby reducing the $O_2(^1\Delta)$ yield. Variations in peak yields at a given specific energy deposition were found to be caused by secondary effects resulting from dilution, pressure, and power level. These secondary effects alter the $O_2(^1\Delta)$ yield by shifting the $O_2(^1\Sigma)/O_2(^1\Delta)$ ratio. A capacitive coupled power deposition model was used to investigate various pulsing schemes. Pulsed discharges were found to produce $O_2(^1\Delta)$ yields that are significantly better than continuous discharges operating at the same conditions. A complete kinetic rate sensitivity analysis shows that these results hold even with moderate uncertainty in the rate coefficient data.

ACKNOWLDEGMENTS

First and foremost, I thank my advisor, Prof. Mark Kushner, for his guidance, support, and insight, without which this work could not have been completed.

I am grateful to the National Science Foundation and the Air Force Office of Scientific Research for their financial support. I am also thankful to Joe Zimmermann, Dr. David Carroll, Prof. Wayne Solomon, and Prof. Joe Verdeyen of the CU-Aerospace group for their collaboration on this project.

I am thankful to the past and present members of the Computational Optical and Discharge Physics Group: Dr. Rajesh Dorai, Dr. Arvind Sankaran, Dr. Pramod Subramonium, Kapil Rajaraman, Richard Moss, Dr. Alex Vasenkov, Ananth Bhoj, Ramesh Arakoni, Ankur Agarwal, Matthew Brenner, Dr. Junquing Lu, and Kelly Collier.

I am most indebted to my wife for her constant support and encouragement throughout the course of my career and education.

TABLE OF CONTENTS

Page

1. INTRODUCTION 1
   - 1.1 Introduction 1
   - 1.2 References 5

2. DESCRIPTION OF THE MODELS 8
   - 2.1 Overview 8
   - 2.2 Zero-Dimensional Plasma Kinetics Model 9
   - 2.3 One-Dimensional Plasma Kinetics and Navier-Stokes Model 13
   - 2.4 Power Deposition Models 18
   - 2.5 Figures 21
   - 2.6 References 23

3. REACTION MECHANISM 25
   - 3.1 Introduction 25
   - 3.2 Plasma and Afterglow Kinetics 25
   - 3.3 Comparison to Experiments 28
   - 3.4 Figures 31
   - 3.5 References 33

4. SCALING OF $O_2(^1\Delta)$ YIELD WITH ENERGY DEPOSITION 35
   - 4.1 Introduction 35
   - 4.2 Typical Discharge Behavior. 35
   - 4.3 Parameterization of Major Process Variables 37
   - 4.4 He Diluent Addition. 39
   - 4.5 Scaling of Effective Yield 43
   - 4.6 Kinetics Sensitivity Analysis 47
   - 4.7 Concluding Remarks 49
   - 4.8 Figures 51
   - 4.9 References 62

5. CONSEQUENCES OF AXIAL TRANSPORT ON $O_2(^1\Delta)$ YIELD. 63
   - 5.1 Introduction 63
   - 5.2 Typical Discharge Behavior 64
   - 5.3 Input Power and Yield Scaling 66
   - 5.4 Advection. 66
   - 5.5 He Dilution 67
   - 5.6 ICP vs. CCP Power Deposition 68
   - 5.7 Pulsed Power Deposition 69
   - 5.8 Discharge Instability 72
   - 5.9 Concluding Remarks 73
   - 5.10 Figures 75
   - 5.11 References 85

6. CONCLUDING REMARKS 86

APPENDIX A. LIST OF REACTIONS FOR He/O_2 PLASMAS 88
A.1 Gas Phase Reaction Mechanism 88
A.2 Wall Reaction Mechanism 94
A.3 References 95

1. INTRODUCTION

1.1 Introduction

Chemical laser operation on the $^2P_{1/2} \rightarrow {}^2P_{3/2}$ transition in atomic iodine has been investigated due to its high efficiency and potential for multi-kilowatt continuous wave (cw) power. The 1.315 μm wavelength couples efficiently with most metals and can be transmitted through fiber optic cable, making the chemical oxygen-iodine laser (COIL) attractive for uses in airborne laser defense systems and nuclear waste site demolition [1-6]. The COIL dissociates gaseous I_2 by collisions with $O_2(^1\Delta)$. Subsequent collisions with $O_2(^1\Delta)$ then excite the atomic iodine in a near resonant transfer to create a population inversion and lasing on the $I(^2P_{1/2}) \rightarrow I(^2P_{3/2})$ transition. In order to achieve the flow rates and temperatures required for high power applications, the gas stream is often expanded through a supersonic nozzle. Conventional COILs generate the $O_2(^1\Delta)$ metastable with yields up to 0.7 using liquid phase chemistry by reaction of Cl_2 in basic H_2O_2 [7]. Although the yield is high, this method is less than optimum for some applications because of the complexity, weight, and operational hazards associated with the liquid chemical storage and pumping systems. Therefore, recent efforts have been investigating the development of all gas phase $O_2(^1\Delta)$ generators [8, 9].

Current research in gas phase $O_2(^1\Delta)$ generation involves capacitive, inductive, and microwave self-sustaining electric discharges in pure O_2 and in mixtures with diluents such as N_2 and He, and e-beam non-self-sustained discharges in similar mixtures [10-16]. The threshold $[O_2(^1\Delta)]/[O_2(^3\Sigma)]$ ratio required for positive laser gain for conventional systems depends on the cavity temperature and can be derived from the equilibrium of the forward and reverse rates of the pumping reaction [17],

$$\frac{\left[O_2(^1\Delta)\right]}{\left[O_2(^3\Sigma)\right]} = 0.67\, exp\left(-\frac{401.4}{T}\right), \quad (1)$$

where the temperature T has units K. At room temperature the threshold ratio is 0.18. Early attempts by Benard and Pchelkin using a microwave discharge as a source of $O_2(^1\Delta)$ produced $[O_2(^1\Delta)]/[O_2(^3\Sigma)]$ fractions of 0.11 [18]. Later, Fournier *et al*. proposed that the maximum achievable excitation fraction in a discharge is 0.135, based on excitation equilibrium calculations and experiments using an electron-beam sustained discharge at 1.15 bar [19].

More recent investigations on electric discharge production of $O_2(^1\Delta)$ have centered on engineering the reduced electric field (E/N) nearer to the optimum value for $O_2(^1\Delta)$ production which, based on calculations of the electron energy distribution for discharges in pure O_2, is ≈10 Td (1 Td = 10^{-17} V cm^2) [11, 14, 20, 21]. This value is too low for self-sustained discharges. In an attempt to circumvent the loss of efficiency of $O_2(^1\Delta)$ excitation that occurs in self-sustained discharges, Hill developed a controlled avalanche discharge method whereby short, high voltage pulses ionize the gas while a lower electric field sustains the discharge between the pulses [10]. This method has been used by Hill to obtain 0.16 yield and has also been investigated by Verdeyen *et al*. [22].

Electron beam sustained discharges have also been investigated by Ionin *et al*. [14]. With the addition of Ar and CO or H_2 to the O_2, they were able to increase the specific energy input obtainable with an e-beam up to about 1.5 eV per molecular component. Their modeling results for non-self-sustained discharges predicted yields up to 0.25 with $O_2(^1\Delta)$ excitation efficiencies of ≈0.4 when using molecular additives such as CO, H_2, or D_2. Inert gas diluents and molecular

additives have also been used with success by Schmiedberger with a hollow cathode radio frequency (rf) jet discharge [12]. At 0.43 Torr, a 0.32 yield was obtained by flowing an $O_2/N_2/NO$ mixture through the discharge jet and then chilling the gas by mixing with a cold Ar/NO_2 stream. However, the pressure was lower than typical high power COIL system pressures.

Moderate yields at higher pressures have been recently achieved by Rakhimova *et al*. and Savin *et al*. [15, 16]. Rakhimova *et al*. performed experiments in a transverse electrode capacitive discharge in pure O_2 and in mixtures with Ar and He from 1-40 Torr [15]. They obtained an $[O_2(^1\Delta)]/[O_2(^3\Sigma)]$ ratio of 0.3 in pure O_2 and 0.4 in mixtures with He and Ar which showed good agreement with a numerical model. Savin *et al*. obtained 0.25-0.30 yield in 1-2 Torr of pure O_2 in a traveling microwave discharge, also obtaining good agreement with a model [16]. Both of these kinetic models include a 3-body $O_2(^1\Delta)$ quenching reaction proposed by Ivanov [11, 15, 16],

$$O + O_2(^1\Delta) + O_2 \rightarrow O + O_2 + O_2 \qquad k = 10^{-32}\ \mathrm{cm^6\ s^{-1}}. \tag{2}$$

Carroll, *et al.* have recently reported positive gain in an electric discharge pumped COIL using a capacitive coupled discharge in He and O_2 at moderate power levels and pressures [23]. In order to reduce the operating E/N of the gas, NO was added at the inlet. In addition, NO_2 was injected downstream of the discharge to scavenge O atoms before the iodine injection point.

In this work, we present results from a computational investigation of $O_2(^1\Delta)$ yields produced by self-sustained discharges in He/O_2 mixtures. A global plasma kinetics model was modified to address one-dimensional steady-state plug flow and was validated against

experiments. The effects of typical discharge variables – mixture, pressure, flow rate, and power – were investigated. We found that yields of $O_2(^1\Delta)$ increase linearly with O_2 specific energy deposition up to a saturation regime at 5-8 eV per molecule before decreasing again as O_2 dissociation begins to dominate the kinetics. We also found that the dissociation fraction reaches 0.5 when the peak $O_2(^1\Delta)$ yield occurs. The dissociation fraction increases monotonically with specific energy deposition, exceeding 0.9 by 20 eV per molecule. However, after correcting for specific energy deposition, the peak yield in the saturation regime is still influenced by composition, power deposition, and pressure. Moderate variations in these parameters cause up to a 50% variation in the peak yield at a given energy deposition. We found that the variations in yield are caused by changes in gas density and mole fractions which affect the $O_2(^1\Delta)$ and $O_2(^1\Sigma)$ kinetics and that the variations are largely independent of E/N.

A one-dimensional (1-D) axial flowing plasma kinetics model was also developed to investigate the consequences of axial transport of mass, momentum, and energy on the $O_2(^1\Delta)$ yield, with specific focus on elongation of the discharge area. Three power deposition models were developed: simplified plug-flow, inductively coupled plasma (ICP), and capacitively coupled plasma (CCP). In addition, a pulsed discharge model was developed to investigate the avalanche discharge proposed by Hill [10]. We found that although the axial transport tends to elongate the plasma glow region, the energy scaling law derived using the global model was still valid. The plasma represented by the ICP model did not significantly extend the coils, while the plasma in the CCP model propagated significantly upstream and downstream of the electrodes. The inclusion of axial transport into the model tended to lower the average electron temperature in the discharge region, raising the $O_2(^1\Delta)$ yield. Other techniques used to lower the average

electron temperature such as pulsing the discharge and the addition of NO were also investigated.

The plasma kinetics and Navier-Stokes transport models used to model the flowing discharge are described in Chapter 2. The gas phase and electron impact reaction kinetics are discussed in Chapter 3. Scaling of $O_2(^1\Delta)$ yield based on the zero-dimensional model is discussed in Chapter 4. The effects of modeling the axial transport with the ICP, CCP, and pulsed plasma models are discussed in Chapter 5. Concluding remarks are in Chapter 6.

1.2 References

1. McDermott, W.E., et al., *An electronic transition chemical laser.* Applied Physics Letters, 1978. **32**(8): p. 469-470.
2. Fujii, H., et al., *Development of high-power chemical oxygen-iodine laser for industrial application.* Journal of Applied Physics, 1990. **67**(9): p. 3948-3953.
3. Elior, A., et al., *Experiment and modeling of a small-scale, supersonic chemical oxygen-iodine laser.* Applied Physics B, 1995. **61**: p. 37-47.
4. Endo, M., et al., *High-Efficiency Operation of Chemical Oxygen-Iodine Laser Using Nitrogen as Buffer Gas.* IEEE Journal of Quantum Electronics, 1998. **34**(3): p. 393-398.
5. Furman, D., et al., *Parametric Study of Small-Signal Gain in a Slit Nozzle, Supersonic Chemical Oxygen-Iodine Laser Operating without Primary Buffer Gas.* IEEE Journal of Quantum Electronics, 2001. **37**(2): p. 174-182.
6. Kodymova, J., et al., *Development of the Chemical Oxygen Iodine Laser (COIL) with chemical generation of atomic iodine.* Applied Physics A: Materials Science & Processing, 2003. **77**(2): p. 331-336.

7. Kodymova, J. and O. Spalek, *Performance Characteristics of Jet-type Generator of Singlet Oxygen for Supersonic Chemical Oxygen-Iodine Laser*. Japanese Journal of Applied Physics, 1998. **37**(1): p. 117-121.

8. Carroll, D.L. and W.C. Solomon. *ElectriCOIL: An Advanced Chemical Iodine Laser Concept*. in *Proceedings of the XIII International Symposium on Gas Flow and Chemical Lasers and High Power Laser Conference*. 2000. Florence, Italy, 18-22 September 2000: The International Society for Optical Engineering (SPIE), Bellingham, WA.

9. Henshaw, T.L., et al., *Recent Experimental Results in the Development of an All Gas Phase Iodine Laser.* AIAA Paper 2000-2424, 2000.

10. Hill, A. *The next generation of controlled avalanche discharge gas lasers*. in *International Conference on Lasers*. 2000. Albuquerque, NM: STS Press.

11. Napartovich, A.P., A. Deryugin, and I. Kochetov, *Discharge production of the singlet delta oxygen for an iodine laser.* Journal of Physics D: Applied Physics, 2001. **34**: p. 1827-1833.

12. Schmiedberger, J. and H. Fujii, *Radio-frequency plasma jet generator of singlet delta oxygen with high yield.* Applied Physics Letters, 2001. **78**(18): p. 2649-2651.

13. Carroll, D.L., et al., *Recent Experimental Measurements of the ElectriCOIL System.* AIAA Paper 2003-4029, 2003.

14. Ionin, A.A., et al., *Non-self-sustained electric discharge in oxygen gas mixtures: singlet delta oxygen production.* Journal of Physics D: Applied Physics, 2003. **36**(8): p. 982-989.

15. Rakhimova, T.V., et al., *Radio-frequency plasma generation of singlet oxygen in O_2 and O_2:Ar(He) mixtures.* AIAA Paper 2003-4306, 2003.

16. Savin, Y.V., et al., *Traveling microwave discharge as a singlet delta oxygen source.* AIAA Paper 2003-4305, 2003.

17. Hon, J.F., et al., *A Heuristic Method for Evaluating COIL Performance.* AIAA Paper 94-2422, 1994.

18. Benard, D.J. and N.R. Pchelkin, *Measurement of $O_2(^1\Delta)$ content in the gaseous effluents of a chemical generator.* Review of Scientific Instruments, 1978. **49**(6): p. 794-796.

19. Fournier, G., et al. *Excitation of singlet oxygen at atmospheric pressure*. in *Proceedings 15th International Conference on Phenomena in Ionized Gases. Part II.* 1981. Minsk.

20. King, D.M., et al. *ElectriCOIL: Preliminary Experiments of Excited Oxygen Generation by RF Discharge*. in *Proceedings of the International Conference on Lasers*. 2000. Albuquerque, NM: STS Press, McLean, VA, 2001.

21. Carroll, D.L., et al., *Recent Electrodynamics Modeling of the ElectriCOIL System.* AIAA Paper 2003-4030, 2003.

22. Verdeyen, J.T., et al. *Diagnostic development for the ElectriCOIL flow system*. in *Proceedings of the Gas and Chemical Lasers and Intense Beam Applications III Conference*. 2002. San Jose, CA, 22-24 January 2002: SPIE, Bellingham, WA.

23. Carroll, D.L., et al., *Measurement of positive gain on the 1315 nm transition of atomic iodine pumped by $O_2(a^1\Delta)$ produced in an electric discharge.* Applied Physics Letters, 2004. **85**(7): p. TBD.

2. DESCRIPTION OF THE MODELS

2.1 Overview

A schematic of a typical electrical discharge COIL device is shown in Fig. 2.1. Oxygen and a diluent such as He are first fed through a quartz tube, where the plasma is sustained by a capacitive or inductive discharge. Additives such as H_2, CO, or NO may also be added, usually to increase the net rate of ionization [1, 2], but will not be discussed here. Powers of 10s to 100s W are deposited into gases flowing at 100s to 1000s of cm/s. Pressures are a few to 10s Torr for O_2 mixtures with mole fractions of 0.03-1 with the balance the inert gas diluent. The gases may be pre-cooled before entering the discharge but usually enter at about 300 K. The discharge section is usually a few tens of cm in length and a few cm in diameter. Following the plasma, the excited oxygen and diluent are fed through a nozzle where I_2 is injected into the flow. To aid in mixing the I_2 secondary flow is typically injected tangentially to the primary flow in the subsonic portion of a supersonic nozzle. The gases then mix, react and cool as they flow through the transonic and supersonic portions of the nozzle. Ideally the gases are cooled to around 140 K as they flow through the laser cavity and are drawn into the exhaust system [3].

GlobalKin, a global plasma kinetics model [4], was modified to simulate steady-state plug flow for this investigation. GlobalKin consists of three main modules: a reaction chemistry and transport module, a Boltzmann equation solver for the electron energy distribution (EED), and an ODE solver. The reaction chemistry and transport module constructs differential equations for the time evolution of species densities and temperatures using results obtained by the Boltzmann solver for electron impact rate coefficients. The differential equations are then integrated by the stiff ODE solver [5]. The zero-dimensional model is discussed in Section 2.2.

Axial transport was modeled by adding the one-dimensional Navier-Stokes equations to the plasma kinetics module of GlobalKin and is discussed in Section 2.3. The three power deposition models – ICP, CCP, and pulsed – were interfaced with the transport and kinetics modules and are discussed in Section 2.4.

2.2 Zero-Dimensional Plasma Kinetics Model

In the zero-dimensional GlobalKin model, the chemistry and transport module first constructs continuity equations for neutral [Eq. (2.1)] and charged [Eq. (2.2)] species, accounting for diffusion to and from the walls and reaction sources,

$$\frac{dN_i}{dt} = -\nabla\left(-\gamma_i D_i \nabla N_i + \sum_j \gamma_j f_{ji} D_j \nabla N_j\right) + S_i - \frac{N_i}{T_g}\frac{dT_g}{dt}, \tag{2.1}$$

$$\frac{dN_i^{\pm}}{dt} = -\nabla\left(-D_{a,i}\nabla N_i\right) + S_i, \tag{2.2}$$

where N_i and $N_i^{\pm}$ are the densities of neutral and charged species i, D_i and $D_{a,i}$ are the regular and ambipolar diffusivities of species i in the mixture, and the sum is over all species. γ_j is the wall reactive sticking coefficient of species j, f_{ji} is the returned fraction of species j as species i from the wall, and S_i is the reaction source term for species i. The last term accounts for excursions of the gas temperature T_g assuming constant pressure operation. The diffusivities are estimated from Lennard-Jones potentials and are calculated for each species as a function of the local gas composition. The ambipolar diffusion coefficients for charged species are based on the instantaneous ion and electron mobilities and diffusivities. Ion mobilities are obtained from

experimental databases [6-9] or estimated based on Langevin values. The electron mobility is obtained from the EED.

For the spatially uniform volumetric model, the second order partial derivatives in the continuity equations can be approximated by substituting the diffusion length Λ, and simplify to

$$\frac{dN_i}{dt} = \frac{1}{\Lambda^2}\left(-\gamma_i D_i N_i + \sum_j D_j N_j \gamma_j f_{ji} \right) + S_i - \frac{N_i}{T_g}\frac{dT_g}{dt}. \qquad (2.3)$$

The source terms for the gas phase and electron impact reactions are obtained from rate expressions for all species,

$$S_i = \sum_j \left(a_{ij}^{\ RHS} - a_{ij}^{\ LHS} \right) k_j \prod_l N_l^{\ a_{lj}^{(LHS)}}, \qquad (2.4)$$

where the a_{ij} are the stoichiometric coefficients of species i in reaction j on the right hand side (RHS) and left hand side (LHS), k_j is the reaction rate coefficient for reaction j, and the product is over all LHS species in reaction j. Rate coefficients are obtained from Arrenhius expressions for the gas phase reactions and from the EED for the electron impact reactions.

For the relatively high pressures (1-100 Torr) typical of COIL discharges, the ions and neutrals are in near thermal equilibrium and can be described by a single temperature. The energy conservation equation for the heavy species includes terms for contributions to gas heating from elastic and inelastic collisions with electrons, from gas phase reaction sources, and from conduction to the walls,

$$\frac{d}{dt}(Nc_P T_g) = \sum_i \frac{3}{2} n_e \nu_{mi} \left(\frac{2m_e}{M_i}\right) k_B (T_e - T_g) + \sum_j n_e k_j N_j \Delta\varepsilon_j$$

$$- \sum_j \Delta H_j + \frac{\kappa}{\Lambda^2}(T_w - T_g) - \frac{d}{dt}\left(\frac{1}{2} M_w N v_x^{\,2}\right), \qquad (2.5)$$

where N is the total gas density and c_P is the mixture averaged heat capacity. ν_{mi} is the momentum transfer collision frequency between electrons and species i, m_e is the electron mass, M_i is the mass of species i, k_B is the Boltzmann constant, T_e is the average electron energy, k_j and $\Delta\varepsilon_j$ are the rate constant and energy contribution from inelastic process j, and ΔH_j is the heat of reaction for process j. The second to last term represents conduction to the wall, where κ is the mixture averaged thermal conductivity and T_w is the wall temperature. The mixture averaged heat capacity and thermal conductivity are estimated from the Lennard-Jones potentials. For some of the most prevalent species in the discharge (He, O_2, and $O_2(^1\Delta)$), the heat capacities are obtained from polynomial correlations for greater accuracy [10]. The last term of Eq. (2.5) accounts for the transfer of internal energy to kinetic energy as the gas expands and the flow velocity v_x increases. In this term, M_w is the mixture averaged molecular weight.

Energy conservation for electrons includes contributions from Joule heating and energy transferred in elastic and inelastic collisions with heavy species,

$$\frac{d}{dt}\left(\frac{3}{2} n_e k_B T_e\right) = P_d - \sum_i \frac{3}{2} n_e \nu_{mi} \left(\frac{2m_e}{M_i}\right) k_B (T_e - T_g) + \sum_l n_e k_l N_l \Delta\varepsilon_l \,, \qquad (2.6)$$

where P_d is the power deposition. In a plug flow model, a circuit parameter (e.g., current density or power) must be specified as a function of distance along the flow direction. We chose to

specify power deposition. When used in this manner, P_d represents the time-averaged power deposition into the electrons over multiple rf cycles. In this regard, the discharge kinetics are analogous to a DC positive column model or inductive discharge with an axially varying E/N as might occur when conductivity is a function of position.

The electron transport coefficients required for Eqs. (2.2)-(2.6) are generated by solving Boltzmann's equation for the EED. The Boltzmann solver is invoked at specified intervals during the simulation to reflect changes in the composition of the gas mixture. The EED is obtained by iterative solution of the two-term spherical harmonic expansion of the Boltzmann equation [11]. The Boltzmann module tabulates average electron energies, transport coefficients, and rate constants for a range of values of E/N and the results are exported to GlobalKin. GlobalKin then interpolates from the tables based on the instantaneous average electron energy obtained by integrating Eq. (2.6) to obtain electron impact reaction rate coefficients and the E/N required to produce the derived average electron energy.

In order to address the flow conditions of the COIL system, the global model was converted to a pseudo one-dimensional plug flow model by introducing the flow velocity v_z and by accounting for gas expansion at constant pressure [Eqs. (2.1) and (2.3)]. The change in flow speed is obtained by conservation of mass flux,

$$\frac{dv_z}{dt} = -\frac{v_z}{\rho}\frac{d\rho}{dt}, \tag{2.7}$$

where the mass density ρ is obtained from the instantaneous mixture averaged molecular weight M_w and the number density N. Integrating the flow velocity gives the location of the initial gas plug as a function of time.

The resulting ordinary differential equations for species densities [Eqs. (2.1) and (2.2)], gas and electron energy [Eqs. (2.5) and (2.6)], and flow velocity [Eq. (2.7)] are normalized in GlobalKin to increase computational efficiency before being integrated. Integration is performed by a double precision variable-coefficient ODE solver developed at LLNL as part of ODEPACK [5].

2.3 One-Dimensional Plasma Kinetics and Navier-Stokes Model

In addition to the plasma kinetics model discussed for the zero-dimensional simulation, the one-dimensional model also includes equations for axial flux of mass, momentum, gas energy, and electron energy. Equations for total mass conservation and species densities (charged and neutral) must be solved,

$$\frac{\partial \rho}{\partial t} + \nabla \cdot \left(\rho \vec{v} \right) = 0 \,, \tag{2.8}$$

$$\frac{\partial N_i}{\partial t} = -\nabla \cdot \left[N_i \left(\vec{v} + \vec{v}_{diff,i} + \vec{v}_{drift,i} \right) \right] + S_i + W_i \,, \tag{2.9}$$

where ρ is the overall density and $\vec{v}$ is the advective velocity. $\vec{v}_{diff,i}$ and $\vec{v}_{drift,i}$ are the diffusive and drift velocities of component *i*, respectively. The reaction source term S_i is obtained from Eq. 2.4, and the radial flux term W_i is obtained similarly to Eq. 2.3,

$$W_i = \frac{1}{\Lambda^2} \left(-D_i N_i \gamma_i + \sum_j D_j N_j \gamma_j f_{ji} \right). \tag{2.10}$$

The diffusion and drift velocities are obtained from the diffusivities D_i and mobilities μ_i,

$$\vec{v}_{diff,i} = -\frac{1}{x_i} D_i \nabla x_i . \tag{2.11}$$

$$\vec{v}_{drift,i} = q_i \mu_i \vec{E}_a , \tag{2.12}$$

where x_i is the mole fraction, q_i is the charge, and μ_i is the mobility of species i. The axial electric field $\vec{E}_a$ was obtained by assuming an ambipolar field, whereby the axial charged fluxes are assumed to sum to zero at any axial point in the discharge. The ambipolar field can then be calculated at any point by

$$\vec{E}_a = -\frac{\sum_i q_i N_i \left(\vec{v} + \vec{v}_{diff,i} \right)}{\sum_i q_i^2 \mu_i N_i} . \tag{2.13}$$

An upwind discretization was utilized for the heavy particle advective flux and drift flux terms to preserve their hyperbolic character and provide some robustness against numerical instabilities. Since the ambipolar field assumption requires a net zero charge flux at any point, the electron density must always equal the net heavy particle charge density for neutral initial conditions and the electron density need not be calculated explicitly via Eq. (2.9).

To obtain the axial gas advective speed, the momentum continuity equation for cylindrical geometry [Eq. (2.14)] may be integrated,

$$\frac{\partial(\rho\vec{v})}{\partial t} + \nabla \cdot (\rho\vec{v}\vec{v} + p + \vec{\tau}) = 0\,, \tag{2.14}$$

$$\nabla \cdot \vec{\tau}_z = \frac{\partial \tau_{zz}}{\partial z} + \frac{4\mu v_{\max}}{R^2}\,, \tag{2.15}$$

$$\tau_{zz} = -\frac{4}{3}\mu \frac{\partial v_z}{\partial z}\,, \tag{2.16}$$

where μ is the mixture averaged viscosity and the divergence of the stress tensor $\vec{\tau}$ is evaluated in the axial direction assuming laminar flow with no-slip boundary conditions at the wall, as represented by Eq. (2.15) and (2.16). The maximum velocity at the center of the discharge v_{max} is obtained from the specified flow conditions and the resulting parabolic axial velocity profile. For typical low Mach number discharges at around 300 K, the pressure variations predicted by Eq. 2.14 will be small compared to the total pressure. If, ultimately, only steady-state conditions are desired, then to save computational time the pressure can be fixed, and the velocity can then be calculated assuming a constant axial mass flux. In either case, the relationship between pressure, density, and temperature are given by the ideal gas equation of state,

$$p = f(N, T_{gas}) = N k_B T_{gas}\,. \tag{2.17}$$

The gas temperature is obtained while considering contributions from the upwinded axial advection and conduction, viscous dissipation, *p*-*V* work, radial conduction, reaction sources, and elastic electron impact,

$$\rho c_P \frac{\partial T}{\partial t} = -\rho \vec{v} c_P \cdot \nabla T - \nabla \cdot \vec{q} - \tau_{zz} \nabla \cdot \vec{v} + \frac{Dp}{Dt} + \frac{\kappa}{\Lambda^2}\left(T_{wall} - T_{gas}\right) + \Delta h_{rxn} + h_e \,, \tag{2.18}$$

$$\vec{q} = -\kappa \nabla T \,, \tag{2.19}$$

$$\Delta h_{rxn} = \sum_j \Delta h_j^\circ k_j \prod_l N_l^{a_{lj}^{(LHS)}} \,, \tag{2.20}$$

$$h_e = \sum_i \frac{3}{2} n_e \nu_{mi} \left(\frac{2m_e}{M_i}\right) k_B \left(T_e - T_g\right). \tag{2.21}$$

The heat capacity c_P and thermal conductivity κ are mixture averaged. If the momentum equation is not integrated (fixed mass flux), then the viscous dissipation and *p*-*V* work terms are assumed to be small and are thus neglected.

The electron temperature is obtained by considering contributions from axial electron flux, joule heating, and elastic and inelastic impacts with heavy neutrals and ions,

$$\frac{\partial\left(\frac{3}{2} n_e k_B T_e\right)}{\partial t} = -\nabla \cdot \vec{q}_e + P_d - h_e + \sum_l n_e k_l N_l \Delta \varepsilon_l \,, \tag{2.22}$$

$$\vec{q}_e = \frac{5}{2} \vec{\Gamma}_e k_B T_e - \lambda_e \nabla k_B T_e \,, \tag{2.23}$$

$$\vec{\Gamma}_e = \mu_e q_e n_e \vec{E} - D_e \nabla n_e \,, \tag{2.24}$$

$$\lambda_e = \frac{5}{2} \frac{n_e k_B T_e}{m_e \nu_{m,avg}} \,, \tag{2.25}$$

$$D_e = \frac{k_B T_e}{m_e \nu_{m,avg}} \,. \tag{2.26}$$

The electron heat flux $\vec{q}_e$ is given by Eq. (2.23) and consists of terms accounting for electron flux and conduction, where $\vec{\Gamma}_e$ is the axial flux given in Eq. (2.24) and λ_e is the electron thermal conductivity given by Eq. (2.25). The flux $\vec{\Gamma}_e$ consists of drift and diffusion, where μ_e is the electron mobility, q_e is the electron charge, $\vec{E}$ is the axial ambipolar electric field, and D_e is the electron diffusivity given by Eq. (2.26). An upwind discretization was used for the drift portion of the electron flux.

The electron transport coefficients used in Eqs. (2.22)-(2.26) are calculated by the offline Boltzmann solver described in Section 2.2. However, since the species mole fractions vary significantly both spatially and temporally, the EED and electron impact rates will be strong functions of position and time as well. Since it would be computationally expensive to evaluate the Boltzmann equation at each grid location for every time step, an approximation is necessary. Therefore, in the one-dimensional scheme the Boltzmann solver calculates the electron transport coefficients as a function of position only. Then, at various time intervals on the approach to the steady solution, the Boltzmann solver is called to update the coefficients at each position along the axis. With the judicious choice of a few update intervals, the time taken for convergence to steady-state is only slightly increased.

The one-dimensional system of equations was then discretized on a mesh having variable spacing. Dirichlet boundary conditions are prescribed for the inlet of the discharge; von Neumann boundary conditions are prescribed at the outlet. When the momentum equation [Eq. (2.14)] is solved, a Dirichlet boundary condition is specified at the outlet to hasten convergence to a steady-state solution. The ODE solver mentioned in Section 2.2 is used with the method of lines to obtain the time-dependent one-dimensional solution.

2.4 Power Deposition Models

Three different methods were used to represent power deposition for specifying the joule heating term in the one-dimensional discharge model [P_d in Eq. (2.22)]: power deposition profile, inductively coupled plasma (ICP), and capacitively coupled plasma (CCP). In the first method, the power deposition is simply specified as a function of distance along the discharge axis and time. As such, the one-dimensional power profile model is analogous to the zero-dimensional power deposition model discussed in Section 2.3.

The ICP model simulates pure inductive coupling from coils wound directly on the OD of the discharge. The axial magnetic field B_i produced at location z_i is the sum of the contributions of the individual coils along the axis [12],

$$B_i = \sum_j^N \frac{2\mu_0 R^2 I}{4r_{ij}^3} \exp\left(\frac{-r_{ij}}{\delta_{ij}}\right), \tag{2.28}$$

where μ_0 is the permeability of free space and the sum is over N coils of radius R, each carrying an rf current I. The field from each coil acts over a distance r_{ij} from the i^{th} point on the axis to a point on the j^{th} coil. The field is reduced by a factor dependent on the skin depth δ_{ij}. The skin depth between z_i on the axis to a point on the j^{th} coil is determined by the average conductivity $\overline{\sigma}_{ij}$ between the two points,

$$\delta_{ij} = \sqrt{\frac{2}{\overline{\sigma}_{ij}\omega\mu_0}}, \tag{2.29}$$

$$\overline{\sigma}_{ij} = \frac{q^2\overline{n}_e}{m_e\overline{\nu}_m}, \tag{2.30}$$

where ω is the angular frequency of the rf current *I*. The average conductivity $\overline{\sigma}_{ij}$ is calculated from the average electron density $\overline{n}_e$ and momentum transfer collision frequency $\overline{\nu}_m$ between the two points. The total power *P* can then be estimated from the $\vec{j} \cdot \vec{E}$ at half radius resulting from an equivalent perfect solenoid,

$$P = \sum_i \left| \sigma_i \vec{E}_i^{\,2} \right|_{RMS} \Delta V_i = \alpha \sum_i \sigma_i B_i^2 \Delta V_i \,, \tag{2.31}$$

where $\left| \sigma_i \vec{E}_i^{\,2} \right|_{RMS}$ is the root-mean-square power deposition from the electric field *E* at the i^{th} location, and ΔV_i is the i^{th} volume element in the discretization. The joule-heating term $\left| \sigma_i \vec{E}_i^{\,2} \right|_{RMS}$ is proportional to $\sigma_i B_i^2$, so a constant of proportionality α is used to convert between the two terms. Since the total power *P* absorbed by the discharge is specified by the problem, α can be calculated and the power depositions $P_{d,i}$ at the grid points can be found,

$$P_{d,i} = \alpha \sigma_i B_i^2 \,. \tag{2.32}$$

For the capacitive discharge model a transmission line approach was utilized, where each mesh cell in the discretization is represented by its associated plasma resistance R_i, as shown in Fig. 2.2. A capacitance $C_{i\pm½}$ is attached at each midpoint and is driven by a sinusoidal voltage $V_{i\pm½}$, where the capacitance is represented by its complex reactance $-j/\omega C_{i\pm½}$ and the voltage is the root-mean-square of the sinusoidal driving voltage. The capacitances are estimated based on

experimental discharge tube geometries. The transmission line model facilitates the simulation of any number and length of internal or external electrodes. Except for the driven electrode, all of the voltages $V_{i\pm½}$ are set to zero (ground). The voltages and currents at each midpoint are described using Ohm's and Kirchoff's laws and the resulting complex system of equations is solved using Thompson's tridiagonal algorithm. The power depositions are then found by

$$P_{d,i} = \Re\left(\frac{V_{R,i}V_{R,i}^{*}}{R_i}\right), \tag{2.33}$$

where $V_{R,i}$ is the complex voltage drop across the plasma resistance R_i at the i^{th} grid point.

With the one-dimensional discharge model, any of the aforementioned power deposition models above may be pulsed using a variable duty cycle waveform. The pulse period, pulse width, rise, and fall times are specified. The total power used in the power profile, ICP, and CCP models discussed above are then scaled by the specified waveform as a function of time. A relative background power level may also be specified, whereby an avalanche-sustained discharge of the type described by Hill may be simulated [13].

2.5 Figures

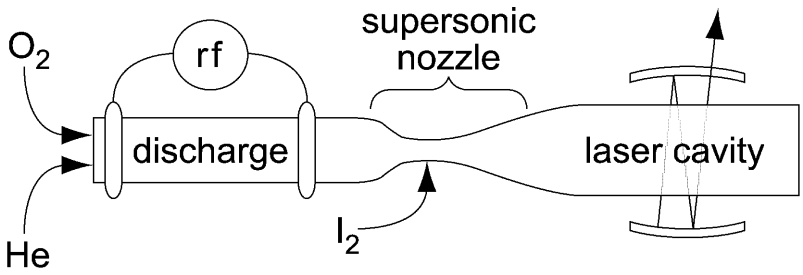

Fig. 2.1. Schematic of typical electric discharge COIL. O_2 is mixed with an inert gas and flowed through the discharge. The gases are then cooled by supersonic expansion before entering the laser cavity.

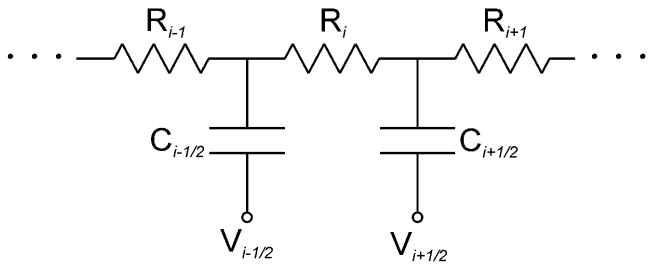

Fig. 2.2. Schematic of transmission line discharge model. Each computational mesh cell has an associated plasma resistance R_i, and each midpoint has an associated capacitance $C_{i\pm½}$ to the drive voltage $V_{i\pm½}$. The drive voltage is set to zero (ground) except at the driven electrode.

2.6 References

1. Ionin, A.A., et al., *Non-self-sustained electric discharge in oxygen gas mixtures: singlet delta oxygen production.* Journal of Physics D: Applied Physics, 2003. **36**(8): p. 982-989.
2. Carroll, D.L., et al., *Measurement of positive gain on the 1315 nm transition of atomic iodine pumped by $O_2(a^1\Delta)$ produced in an electric discharge.* Applied Physics Letters, 2004. **85**(7): p. TBD.
3. Carroll, D.L., et al. *Recent Work on the Development of an Electric Discharge Oxygen Iodine Laser*. in *XIV International Symposium on Gas Flow and Chemical Lasers and High Power Laser Conference*. 2002. Wroclaw, Poland: SPIE.
4. Dorai, R., K. Hassouni, and M.J. Kushner, *Interaction between soot particles and NO_x during dielectric barrier discharge plasma remediation of simulated diesel exhaust.* Journal of Applied Physics, 2000. **88**: p. 6060-6071.
5. Brown, P.N., G.D. Byrne, and A.C. Hindmarsh, *VODE, A Variable - Coefficient ODE Solver.* SIAM Journal on Scientific and Statistical Computing, 1989. **10**(5): p. 1038-1051.
6. Ellis, H.W., et al., *Transport properties of gaseous ions over a wide energy range.* Atomic Data and Nuclear Data Tables, 1976. **17**: p. 177-210.
7. Ellis, H.W., et al., *Transport properties of gaseous ions over a wide energy range. Part II.* Atomic Data and Nuclear Data Tables, 1978. **22**: p. 179-217.
8. Ellis, H.W., et al., *Transport properties of gaseous ions over a wide energy range. Part III.* Atomic Data and Nuclear Data Tables, 1984. **31**: p. 113-151.
9. Viehland, L.A. and E.A. Mason, *Transport properties of gaseous ions over a wide energy range.* Atomic Data and Nuclear Data Tables, 1995. **60**: p. 37-95.

10. Felder, R.M. and R.W. Rousseau, *Elementary Principles of Chemical Processes*. 1999: Wiley, John and Sons, Inc.

11. Rockwood, S.D., *Elastic and Inelastic Cross Sections for Electron-Hg Scattering from Hg Transport Data.* Physical Review A, 1973. **8**(5): p. 2348-2358.

12. Tipler, P.A., *Physics for Scientists and Engineers*. 3rd edition ed. 1991, New York: Worth Publishers.

13. Hill, A. *The next generation of controlled avalanche discharge gas lasers*. in *International Conference on Lasers*. 2000. Albuquerque, NM: STS Press.

3. REACTION MECHANISM

3.1 Introduction

The reaction mechanism used in this investigation involves reactions in the gas phase discharge and afterglow as well as recombination and quenching reactions on the discharge tube walls. The species in the mechanism include ground state neutrals O_2, O, O_3, and He; vibrational and electronic states $O_2(v)$, $O_2(a^1\Delta)$, $O_2(b^1\Sigma)$, $O(^1D)$, $O(^1S)$, and $He(^2S)$; and ions O_2^+, O^+, He^+, O_2^-, O^-, and O_3^-. ($O_2(v)$ represents the total vibrational population consisting of the first four vibrational levels of O_2.) The complete gas phase reaction mechanism is shown Appendix A.1. Wall reactions are listed in Appendix A.2. Typical densities and temperatures are shown in Fig. 3.1 (to be discussed in full in Chapter 4). The typical discharge and reaction mechanism are discussed in Section 3.2. GlobalKin results are compared with various experimental results in Section 3.3.

3.2 Plasma and Afterglow Kinetics

Electron impact reactions dominate the kinetics in the discharge region. At the discharge inlet, where only ground state O_2 and He are present, the O_2 is excited and dissociated, mainly by the four reactions,

$$e + O_2 \rightarrow O_2(^1\Delta) + e, \tag{3.1}$$

$$e + O_2 \rightarrow O(^1D) + O + e, \tag{3.2}$$

$$e + O_2 \rightarrow O + O + e, \tag{3.3}$$

$$e + O_2 \rightarrow O_2(^1\Sigma) + e. \tag{3.4}$$

In the first section of the discharge, most of the $O_2(^1\Delta)$ is produced by direct electron impact [Eq. (3.1)]. However, the rates of the dissociation reactions [Eqs. (3.2), (3.3)] are also large in the discharge, producing large densities of O atoms. These atoms are then excited to $O(^1D)$ by electron impact, thereby creating more $O_2(^1\Delta)$ through a sequence of collisions with O_2,

$$O(^1D) + O_2 \rightarrow O + O_2(^1\Sigma) \qquad k = 2.0\times10^{-11}\ \text{cm}^3\ \text{s}^{-1}\ [1], \tag{3.5}$$

$$O + O_2(^1\Sigma) \rightarrow O + O_2(^1\Delta) \qquad k = 7.2\times10^{-14}\ \text{cm}^3\ \text{s}^{-1}\ [1], \tag{3.6}$$

where k is the rate coefficient at 300 K.

As the $O_2(^1\Delta)$ density increases in the downstream portion of the discharge, processes which remove $O_2(^1\Delta)$ through excitation to upper states, through dissociation, and through superelastic de-excitation to the ground state begin to dominate the kinetics,

$$e + O_2(^1\Delta) \rightarrow O_2(^1\Sigma) + e, \tag{3.7}$$

$$e + O_2(^1\Delta) \rightarrow O(^1D) + O + e, \tag{3.8}$$

$$e + O_2(^1\Delta) \rightarrow O + O + e, \tag{3.9}$$

$$e + O_2(^1\Delta) \rightarrow O_2 + e. \tag{3.10}$$

These processes produce more long lived O atoms and deplete the O_2 available for excitation to $O_2(^1\Delta)$. In this downstream region the discharge becomes less efficient at producing $O_2(^1\Delta)$, and atomic O is produced instead.

Ozone is also created early in the discharge, primarily through collisions of $O_2(^1\Delta)$ and O^- ions and through a three-body reaction,

$$O^- + O_2(^1\Delta) \rightarrow O_3 + e \qquad k = 3.0\times10^{-10}\ \text{cm}^3\ \text{s}^{-1}\ [2], \tag{3.11}$$

$$O + O_2 + M \rightarrow O_3 + O_2 + M \qquad k = 6.0\times10^{-34}\ \text{cm}^6\ \text{s}^{-1}\ [3]. \tag{3.12}$$

However, later in the discharge region the $O_2(^1\Sigma)$ density becomes large enough so that the dissociation reaction,

$$O_2(^1\Sigma) + O_3 \rightarrow O + O_2 + O_2 \qquad k = 7.3\times10^{-12}\ \text{cm}^3\ \text{s}^{-1}\ [3], \tag{3.13}$$

controls the O_3 density, keeping the O_3 fraction in the ppm range throughout the discharge.

In the early afterglow, there is a brief increase in $O_2(^1\Delta)$ density as the remaining $O_2(^1\Sigma)$ is de-excited by O atoms [Eq. (3.6)]. The $O_2(^1\Delta)$ metastable has a 64.4 minute radiative lifetime [4], so high densities persist far downstream in the afterglow. The dominant afterglow reactions reduce the $O_2(^1\Delta)$ density through collisions with O and O_3, and through pooling reactions,

$$O_2(^1\Delta) + O \rightarrow O_2 + O \qquad k = 2.0\times10^{-16}\ \text{cm}^3\ \text{s}^{-1}\ [5], \tag{3.14}$$

$$O_2(^1\Delta) + O_3 \rightarrow O_2 + O_2 + O \qquad k = 4.0\times10^{-15}\ \text{cm}^3\ \text{s}^{-1}\ [6], \tag{3.15}$$

$$O_2(^1\Delta) + O_2(^1\Delta) \rightarrow O_2 + O_2 \qquad k = 1.4\times10^{-17}\ \text{cm}^3\ \text{s}^{-1}\ [5], \tag{3.16a}$$

$$O_2(^1\Delta) + O_2(^1\Delta) \rightarrow O_2(^1\Sigma) + O_2 \qquad k = 1.4\times10^{-17}\ \text{cm}^3\ \text{s}^{-1}\ [5]. \tag{3.16b}$$

Ozone is rapidly depleted immediately after the discharge as its primary source [Eq. (3.11)] is diminished by O^- recombination. Later in the afterglow, the O_3 density again increases. $O_2(^1\Sigma)$, the dominant quencher of O_3 [Eq. (3.13)] is depleted by reactions with O atoms [Eq. (3.6)], thereby allowing the weaker 3-body association reaction [Eq. (3.12)] to repopulate O_3.

A simple wall reaction mechanism describes species diffusing to and returning from the walls. In this mechanism, all ions are neutralized at the wall and return as ground state species. Excited species are quenched on the walls with the probabilities given in Appendix A.2, and return to the gas in the ground state. Some of the atomic O reaching the wall recombines to form ground state O_2.

3.3 Comparison to Experiments

GlobalKin has been validated with a similar reaction mechanism for microwave discharges by Zimmerman *et al*. [7] using results from Benard and Pchelkin [8], and for rf discharges by Carroll *et al*. [9], using results from capacitive discharges at 2-10 Torr in Ar/He/O_2 mixtures. Good agreement was obtained between the model and experimental results in both cases. Results from GlobalKin using the reaction mechanism discussed in this paper are shown in Fig. 3.2 with experimental results from Carroll *et al*. [9]. The gas temperature was experimentally obtained from the $O_2(^1\Sigma)$ rotational spectra. GlobalKin predicts the gas temperature well despite the simplicity of the radial heat conduction model. The predicted peak gas temperature is somewhat lower than the experiment because GlobalKin assumes constant temperature at the discharge tube wall. Due to the difficulty of experimentally obtaining an absolute $O_2(^1\Delta)$ or $O_2(^1\Sigma)$ density, the $O_2(^1\Sigma)$ density from GlobalKin is compared on a relative basis to optical emission sidelight from $O_2(^1\Sigma)$. The fast decay of the $O_2(^1\Sigma)$ density predicted by

GlobalKin is markedly different than the slower decay measured in the experiment. The kinetic model developed Savin *et al*. in agreement with their experimental results also predicts a fast decay in $O_2(^1\Sigma)$ density [10]. The rate of decay of $O_2(^1\Sigma)$ in the afterglow is a current topic of discussion.

Comparisons were also made to reported absolute $O_2(^1\Delta)$ densities. The difficulty of experimentally obtaining absolute $O_2(^1\Delta)$ densities is apparent from the broad range of reported $O_2(^1\Delta)$ yields as a function of specific energy. Reported values of $O_2(^1\Delta)$ yield per eV deposited into inlet O_2 molecules range from 0.01 eV^{-1} [11] to 0.39 eV^{-1} [12]. GlobalKin predicts yields between the results reported by Benard and Pchelkin [8] and Savin *et al*. [10], from 0.06-0.08 eV^{-1}. These values are near the median of the results discussed here which correspond to the peak $O_2(^1\Delta)$ yield being at 5-8 eV per molecule of inlet O_2. These scalings will be discussed further in Chapter 4.

There are two definitions of $O_2(^1\Delta)$ yield currently used when discussing COIL systems. The first is the traditional method used when characterizing conventional liquid phase $O_2(^1\Delta)$ generation systems,

$$Y = \frac{[O_2(^1\Delta)]}{[O_2(^3\Sigma)] + [O_2(^1\Delta)]}, \tag{3.17}$$

where Y is the $O_2(^1\Delta)$ yield and the denominator includes only the ground state $O_2(^3\Sigma)$ and excited $O_2(^1\Delta)$ species. Eq. (3.17) accurately describes $O_2(^1\Delta)$ yields for conventional systems because yields are high and there is little dissociation or excitation to other states [13]. Eq. (3.17) is also convenient when comparing to the threshold yield, which can be derived from Eqs.

(1.1) and (3.17). However, to describe the $O_2(^1\Delta)$ yield in an electric discharge COIL, dissociation and populated electronic states should be included,

$$Y = \frac{[O_2(^1\Delta)]}{[O_2(^3\Sigma)] + [O_2(v)] + [O_2(^1\Delta)] + [O_2(^1\Sigma)] + 0.5[O] + 1.5[O_3]}. \quad (3.18)$$

The denominator of Eq. (3.18) includes all major oxygen species in the discharge on an O_2 equivalent basis, giving the yield *Y* as the fractional conversion of inlet O_2 to $O_2(^1\Delta)$. The latter method for computing yield [Eq. (3.18)] was used in this investigation.

3.4 Figures

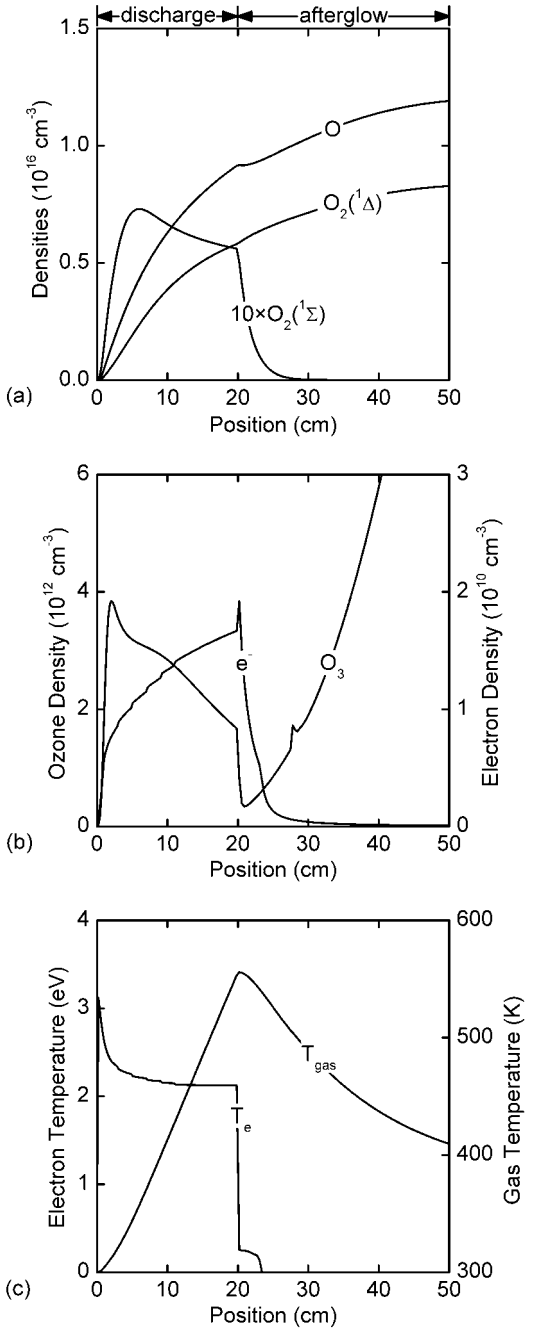

Fig. 3.1. Plasma properties for the base case (O_2 at 3 Torr: L = 20 cm, $v_{x,in}$ = 1000 cm/s, P_d = 0.5 W/cm^3). (a) $O_2(^1\Delta)$, $O_2(^1\Sigma)$, and O atom densities. (b) O_3 and electron densities. (c) Electron and gas temperatures.

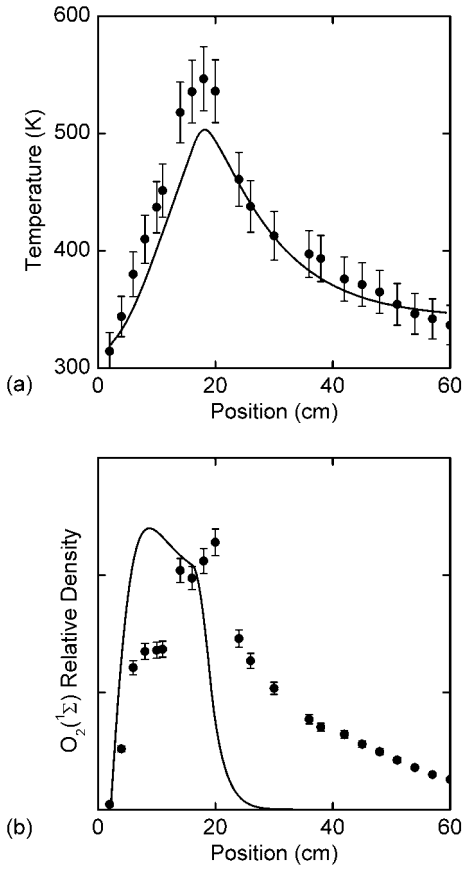

Fig. 3.2. Comparison of computed results with experiments by Carroll *et al*. for 5 mmol/s of pure O_2 at 2 Torr flowing through a 4.83 cm ID quartz tube [9]. 265 W was deposited between electrodes spaced 30 cm apart.. (a) Gas temperature as a function of position. GlobalKin predicts gas temperature well with a simple heat conduction model. (b) $O_2(^1\Sigma)$ relative density as a function of position.

3.5 References

1. Atkinson, R., et al., *Evaluated Kinetic and Photochemical Data for Atmospheric Chemistry: Supplement V.* Journal of Physical and Chemical Reference Data, 1997. **26**: p. 521-1011.
2. Ikezoe, Y., et al. *Gas Phase Ion-Molecule Reaction Rate Constants Through 1986*. in *Ion Reaction Research Group of the Mass Spectroscopy Society of Japan*. 1987. Tokyo, Japan.
3. Choo, K.W. and M.T. Leu, *Rate Constants for the Quenching of Metastable $O_2(^1\Sigma_g^+)$ Molecules.* International Journal of Chemical Kinetics, 1985. **17**: p. 1155.
4. Newman, S.M., et al., *Temperature and Pressure Dependence of Line Widths and Integrated Adsorption Intensities for the $O_2a^1\Delta_g - x^3\Sigma_g^-$ (0,0) Transition.* Journal of Physical Chemistry A, 2000. **104**(42): p. 9467-9480.
5. Herron, J.T. and D.S. Green, *Chemical Kinetics Database and Predictive Schemes for Nonthermal Humid Air Plasma Chemistry. Part II. Neutral Species Reactions.* Plasma Chemistry and Plasma Processing, 2001. **21**(3): p. 459-481.
6. Atkinson, R., et al., *Evaluated Kinetic and Photochemical Data for Atmospheric Chemistry: Supplement VI (O_x, HO_x, NO_x, SO_x).* Journal of Physical and Chemical Reference Data, 1997. **26**: p. 1329-1499.
7. Zimmerman, J.W., et al. *Electrodynamic modeling of the ElectriCOIL system*. in *Proceedings of Gas and Chemical Lasers and Intense Beam Applications IV*. 2003. San Jose, California: SPIE, Bellingham, WA.
8. Benard, D.J. and N.R. Pchelkin, *Measurement of $O_2(^1\Delta)$ content in the gaseous effluents of a chemical generator.* Review of Scientific Instruments, 1978. **49**(6): p. 794-796.

9. Carroll, D.L., et al., *Recent Experimental Measurements of the ElectriCOIL System.* AIAA Paper 2003-4029, 2003.

10. Savin, Y.V., et al., *Traveling microwave discharge as a singlet delta oxygen source.* AIAA Paper 2003-4305, 2003.

11. Rakhimova, T.V., et al., *Radio-frequency plasma generation of singlet oxygen in O_2 and O_2:Ar(He) mixtures.* AIAA Paper 2003-4306, 2003.

12. Verdeyen, J.T., et al. *Diagnostic development for the ElectriCOIL flow system*. in *Proceedings of the Gas and Chemical Lasers and Intense Beam Applications III Conference*. 2002. San Jose, CA, 22-24 January 2002: SPIE, Bellingham, WA.

13. Kodymova, J. and O. Spalek, *Performance Characteristics of Jet-type Generator of Singlet Oxygen for Supersonic Chemical Oxygen-Iodine Laser.* Japanese Journal of Applied Physics, 1998. **37**(1): p. 117-121.

4. SCALING OF $O_2(^1\Delta)$ YIELD WITH ENERGY DEPOSITION

4.1 Introduction

The zero-dimensional GlobalKin model was used to simulate axially flowing discharges in O_2 and He mixtures. The speed and ease of use of the zero-dimensional model facilitated a large-scale investigation of the effects of the modeling parameters on the $O_2(^1\Delta)$ yields. Thus, a parameterization of the independent input variables flow velocity, pressure, power, and mixture was completed to determine their effects on $O_2(^1\Delta)$ yields. These variables interact to give different specific energy depositions on an inlet O_2 basis. The $O_2(^1\Delta)$ yield was found to be a strong function of the specific energy deposition, but a weaker function of the four variables acting individually. After discussion of the plasma parameters for a typical discharge in Section 4.2, the specific energy deposition scaling is discussed in Section 4.3. The effects of adding a diluent such as He are discussed in Section 4.4. When the $O_2(^1\Sigma)$ density is also included in the calculation of the $O_2(^1\Delta)$ yield to produce an effective yield, the independent variables have even weaker individual effects. The results of a parameterization with respect to the effective yield are discussed in Section 4.5. A complete sensitivity analysis of rate coefficients was performed to determine the effects of uncertainty in the rate data. The results of the analysis are presented in Section 4.6. Concluding remarks for the zero-dimensional study are in Section 4.7.

4.2 Typical Discharge Behavior

The base case uses conditions similar to experiments performed by others [1]. The electric discharge COIL experiments typically use a 4.83 cm ID Pyrex discharge tube with an axial capacitive or inductive discharge over 20-30 cm of length. Pressures range from a few to

10s of Torr, with flow velocities of 100s to 1000s of cm/s, giving residence times on the order of a few to 10s of ms [1]. Absorbed power in the discharge ranges from 10s to 100s W, corresponding to power depositions from 0.01 to 1 W/cm^3. The base case has a 20 cm discharge length, pure O_2 at 3 Torr, and power deposition of 0.5 W/cm^3.

Densities and temperatures as a function of position are shown in Fig. 4.1. The $O_2(^1\Delta)$ density rises in the discharge primarily by direct electron impact excitation from ground state O_2 [Eq. (3.1)], while the O density increases due to dissociation from the ground state [Eqs. (3.2) and (3.3)]. The O atom yield on an O_2 equivalent basis is roughly equal to the $O_2(^1\Delta)$ yield for conditions providing peak $O_2(^1\Delta)$ yield (5-8 eV/molecule), giving O densities twice that of the $O_2(^1\Delta)$ density. (Note that the conditions for Fig. 4.1 are less than optimum.) The $O_2(^1\Sigma)$ density also initially rises due to electron impact excitation [Eq. (3.4)], but then plateaus after the O density becomes large enough so that the rate of quenching by O atoms [Eq. (3.6)] balances the rate of excitation. This is not intrinsically bad as the product of the quenching is dominantly $O_2(^1\Delta)$. Some O_3 is also produced in the discharge region by reaction of O^- and $O_2(^1\Delta)$ [Eq. (3.11)], but the density also saturates. The source of O_3 changes to O + O_2 association as the O density increases and quenching by $O_2(^1\Sigma)$ [Eq. (3.13)] balances the source. The gas temperature rises nearly 150 K in the pure O_2 discharge, primarily through Frank-Condon heating, which emphasizes the need to cool the gas flow if laser gain is to be achieved.

The electron density quickly rises to 0.6×10^{10} cm^{-3} (at 3 Torr) early in the discharge and then slowly increases to 1.5×10^{10} cm^{-3} by the end of the discharge. The increase in n_e while power is constant is largely due to the dissociation of O_2 and thermal expansion of the gas, both of which reduce the power dissipation (eV/cm^3 s) per electron. The electron density then increases to compensate. The small spike in n_e at the end of the discharge results from loss

processes decreasing at a higher rate than ionization processes as T_e decreases. The electron temperature peaks before falling to a stationary value near 2 eV as the electron density saturates.

The initial spike in electron temperature is partly due to the simplicity of the plug flow model, which does not account for upstream electron transport and thus assumes a fairly low electron density (10^5 cm^{-3}) at the beginning of the power deposition envelope. A finite power deposited into a small inventory of electrons requires a large T_e to dissipate. T_e thermalizes quickly at the end of the discharge region. The small knee in the electron temperature at the end of the discharge results from superelastic electron heating, primarily from the vibrational state $O_2(v=1)$ at 0.19 eV. Electron impact excitation is unimportant downstream for these conditions though electron collision quenching persists for another 10-15 cm.

In the afterglow, $O_2(^1\Delta)$ and O densities continue to rise as the gas cools. Conversely, the most important two reaction pathways in the afterglow are $O_2(^1\Delta)$ quenching by O atoms [Eq. (3.14)] and O_3 formation [Eq. (3.12)], which reduce the $O_2(^1\Delta)$ and O mole fractions slightly even though the gas density is increasing. Both the $O_2(^1\Delta)$ metastable and the O atom densities persist far downstream, with no appreciable changes in density by 50 cm downstream of the discharge inlet (30 cm from the end of the discharge). The $O_2(^1\Delta)$ yield for this case was 0.108 at the end of the discharge and 0.111 at the end of the flow tube (30 cm downstream of the discharge).

4.3 Parameterization of Major Process Variables

With the goal of maximizing the yield of $O_2(^1\Delta)$, a full factorial experiment was designed to investigate the effects of discharge parameters. The parameters of primary interest for laboratory COIL experiments are pressure, flow velocity, He/O_2 ratio, and power deposition.

Other parameters such as the length of the discharge, the discharge tube wall temperature, and the discharge diameter are also of interest, but these were deemed less important than the primary four variables because of their more easily predictable effects.

A 4 factor, 4 level full factorial computational experiment (256 cases) was run. Inlet velocities ranged from 500-5000 cm/s, total pressures from 1-20 Torr, power depositions from 0.1-1.5 W/cm^3, and O_2 fractions in He from 0.03-1. Although this design allows resolution of linear effects, 2-, 3-, and 4-way interactions, all four variables were expected to have strong interactions that influence $O_2(^1\Delta)$ yield by changing the net amount of energy deposited into the oxygen species. Therefore, the expected 4-way interaction of the independent variables was accounted for by defining a new variable, the specific energy deposition, $\overline{E}_d$ which, like the yield, is calculated on a molecular oxygen basis,

$$\overline{E}_d = \frac{E_d}{[O_2(^3\Sigma)] + [O_2(v)] + [O_2(^1\Delta)] + [O_2(^1\Sigma)] + 0.5[O] + 1.5[O_3]}, \qquad (4.1)$$

where E_d is the total energy deposited into the gas in eV/cm^3 and $\overline{E}_d$ is the total energy deposited in eV/molecule on an O_2 equivalent basis. Implicit in Eq. (4.1) is the assumption that little energy is deposited into the He species, which as we show below, is a reasonable assumption for moderate mole fractions of O_2. The choice of values for the independent variables (inlet velocity, pressure, power deposition, and O_2 fraction) results in $\overline{E}_d$ ranging from 0.004-265 eV for a 20 cm discharge. Because $\overline{E}_d$ has a much stronger and clearer effect on $O_2(^1\Delta)$ yield than any of the four independent variables taken separately, we propose a scaling law giving the $O_2(^1\Delta)$ yield Y as a function of the specific energy deposition $\overline{E}_d$,

$$Y = f\left(\overline{E}_d\right). \tag{4.2}$$

Results of the full factorial experiment for the scaling of $O_2(^1\Delta)$ and O yields with $\overline{E}_d$ are shown in Fig. 4.2. The $O_2(^1\Delta)$ yield is at the exit of the discharge region. $O_2(^1\Delta)$ yield increases almost linearly with $\overline{E}_d$ at low specific energy depositions before saturating with yields of ≈ 0.3 by 5-8 eV/molecule. Since the $O_2(^1\Delta)$ state lies at 0.977 eV, this corresponds to 0.04-0.06 excitation energy efficiency into $O_2(^1\Delta)$ in the peak yield range of 5-8 eV/molecule.

As more energy is deposited into the oxygen species, dissociation increases [see Fig. 4.2(b)], reducing the available O_2 that can be excited to $O_2(^1\Delta)$. The depletion of $O_2(^1\Delta)$ by electron impact processes also becomes important. As the $O_2(^1\Delta)$ yield peaks at 5-8 eV/molecule, dissociation into O atoms has reached 50%. O yield continues to monotonically increase as specific energy deposition rises to 20 eV. By 30 eV, almost all of the oxygen is dissociated, and further increases in $\overline{E}_d$ serve only to further excite and ionize the O species. This emphasizes the importance of including O density when discussing $O_2(^1\Delta)$ yields [Eq. (3.18)]. Although these results show that $O_2(^1\Delta)$ yields follow the scaling law [Eq. (4.2)], there is a large variation in yields for $\overline{E}_d$ = 5-8 eV/molecule, suggesting secondary effects linked to changes in the independent variables.

4.4 He Diluent Addition

The implied E/N as a function of axial position in pure O_2 is shown in Fig. 4.4(a). The E/N is large at the leading edge of the plasma zone for two major causes. First, the electron

density is initially small (10^8 cm^{-3}). Dissipating a finite power by a small inventory of electrons requires a large power dissipation per electron. This is accomplished by having a large T_e which requires a large E/N, as shown in Fig. 4.1(c). (Analogously, the conductivity is small and so to dissipate a finite power, the electric field must be large.) The large T_e avalanches the plasma, thereby increasing the electron density. As the electron density increases, the power dissipation per electron decreases, thereby requiring a lower T_e and smaller E/N. Second, the gas composition at the leading edge of the plasma zone has few excited states and so electron impact ionization is almost exclusively from ground state species, thereby required a higher T_e and larger E/N. As the excited state inventory builds, the efficiency of ionization increases, thereby required a lower T_e and smaller E/N to sustain the plasma.

In electric discharge COIL systems an inert diluent such as He is often added to the O_2 to reduce the temperature rise in the discharge and aid the gas dynamics by increasing the system pressure. The diluent also reduces the amount of flow expansion caused by O_2 dissociation, which in turn increases the residence time in discharge region. The increased residence time leads to higher specific energy deposition with a consequent rise in yield.

When adding He to the discharge at constant O_2 partial pressure (thereby increasing total pressure) and constant specific energy deposition, $O_2(^1\Delta)$ yields can increase, as shown in Fig. 4.3. At low $\overline{E}_d$, adding He has little effect. In the range of $\overline{E}_d$ = 5-8 eV/molecule where the yield peaks, adding He can increase the yield several percent. When the He fraction is above ≈0.8 more specific energy deposition is required to obtain the peak yield. This additional energy is largely deposited into He through electron momentum transfer collisions. It has been suggested that the addition of an inert diluent such as He may promote higher $O_2(^1\Delta)$ yields by allowing the discharge to operate at a more favorable E/N for $O_2(^1\Delta)$ production [1-3]. For our

particular conditions the addition of He produces a less favorable E/N than does pure O_2, and a different mechanism is responsible for the increased yields.

Adding He to a O_2 discharge does reduce the quasi-steady-state E/N, as shown in Fig. 4.4(a). E/N rises rapidly at the discharge inlet to avalanche the low electron density before falling to a quasi-steady-state value, showing the same trend as the electron temperature in Fig. 4.1(c). The quasi-steady E/N is approached as the rate of ionization balances the rate of loss by diffusion to the walls, attachment and recombination. The ionization rate exceeds the rate of loss by collisions by the diffusion loss. As such, in the limit of there being no charged particle losses to the walls, the quasi-steady E/N would correspond to a net ionization rate by collisions of zero. The quasi-steady-state E/N predicted by GlobalKin for discharges in pure O_2 at 3 Torr is $\approx$40 Td. Napartovich *et al*. also calculated a quasi-steady value of 40 Td for pure O_2 at 10 Torr using a DC positive column model [2]. For typical He/O_2 ratios near 4/1, the discharge operates from 20-30 Td, and E/N falls to below 10 Td for He/O_2 = 99/1. As the O_2 partial pressure is held constant, adding He increases the total pressure. Therefore a portion of the reduction in E/N reflects reduced charged particle loss by diffusion.

In order for the addition of He to increase the yield of $O_2(^1\Delta)$ the fraction of power dissipated in electron impact excitation of $O_2(^1\Delta)$ should increase as E/N decreases. The fraction of power expended in excitation of $O_2(^1\Delta)$ [Eq. (3.1)] for mixtures of O_2 and He at the inlet conditions is shown in Fig. 4.4(b). For pure O_2, the maximum power dissipated into $O_2(^1\Delta)$ occurs near 10 Td, but the discharge operates near 40 Td. As He is added, the E/N at which the $O_2(^1\Delta)$ excitation is a maximum decreases as does the operating E/N while the fraction of power dissipated into $O_2(^1\Delta)$ decreases. The reduction in operating E/N made possible by the addition of He does not fully counteract the decrease in the fraction of power dissipated in $O_2(^1\Delta)$

excitation. Therefore, for these conditions the addition of He actually *decreases* the efficiency of electron impact excitation of O_2 to $O_2(^1\Delta)$.

Further along the discharge, after some $O_2(^1\Delta)$ has formed, the net fraction of power to $O_2(^1\Delta)$ by direct electron impact decreases, as the rate of electron quenching collisions with $O_2(^1\Delta)$ through upward excitation [Eq. (3.7)], dissociation [Eqs. (3.8)-(3.9)], and superelastic de-excitation [Eq. (3.10)] begin to dominate. For example, the fraction of power dissipated in $O_2(^1\Delta)$ excitation after 15% of the inlet O_2 has been converted to $O_2(^1\Delta)$ is shown in Fig. 4.4(c). In addition to the loss process for $O_2(^1\Delta)$, there is a significant density of O at this time which also dissipates power. Below 10 Td, at high He fractions the $O_2(^1\Delta)$ density is high enough that more electron impact events remove power from $O_2(^1\Delta)$ by superelastic collisions [Eq. (3.10)] than deposit power by direct electron impact, resulting in negative power fractions to $O_2(^1\Delta)$. Sustaining of the $O_2(^1\Delta)$ density at this juncture requires indirect processes such as excitation and subsequent quenching of $O_2(^1\Sigma)$. The fraction of power into $O_2(^1\Delta)$ continues to decrease as the yield increases for self-sustained discharges with He addition, as adding He reduces the rate of direct electron impact.

Inert gases are often added to the discharge to cool the flowing O_2 to make the laser gain kinetics more favorable. The gas cooling also increases the residence time, in turn raising the specific energy deposition at a given power. The higher average gas density also reduces diffusion losses of both excited states and charged particles. The maximum gas temperature is shown in Fig. 4.5(a) as a function of O_2 mole fraction and $\overline{E}_d$ (O_2 partial pressure is fixed). Due to the increase in heat capacity and thermal conductivity that occurs with He addition, the peak gas temperature decreases with He addition. For example, at $\overline{E}_d$ = 8 eV, T_g can be reduced to

<1000 K with 90% He addition. Although the dominant effect of He addition is to increase the residence time, the gas density also increases relative to the pure O_2 case. Both the reduction in temperature and the net increase in density influence many of the rates in the reaction mechanism, which on the average increases $O_2(^1\Delta)$ yield. For example, $O_2(^1\Delta)$ yield is shown in Fig. 4.5(b) as a function of O_2 fraction and $\overline{E}_d$ when the gas temperature is held constant at 300 K. Yields are significantly higher than when including the gas dynamics (see Fig. 4.3), but the dependence on He fraction is less pronounced as the peak yield increases.

4.5 Scaling of Effective Yield

The disposition of $O_2(^1\Sigma)$ is an important consideration in determining the ultimate $O_2(^1\Delta)$ yield. In optimistic scenarios the vast majority of $O_2(^1\Sigma)$ can be converted to $O_2(^1\Delta)$ in the downstream region by quenching collisions, principally with O atoms. In this regard we can define an effective yield Y' which includes the contribution of $O_2(^1\Sigma)$:

$$Y' = \frac{[O_2(^1\Delta)] + [O_2(^1\Sigma)]}{[O_2(^3\Sigma)] + [O_2(v)] + [O_2(^1\Delta)] + [O_2(^1\Sigma)] + 0.5[O] + 1.5[O_3]} . \qquad (4.3)$$

Effective yield Y' is shown in Fig. 4.6(a) for the same conditions as Fig. 4.3. Up to the value of $\overline{E}_d$ in which peak yield is obtained (5-8 eV/molecule), there is little dependence of yield on mixture. This result suggests that there is a relatively constant dependence of the combined densities of $O_2(^1\Delta)$ and $O_2(^1\Sigma)$ on energy deposition and that the addition of He serves primarily to partition the densities more in favor of $O_2(^1\Delta)$.

The density of $O_2(^1\Sigma)$ at high $O_2(^1\Delta)$ yields is dominated by an equilibrium between quenching by O atoms [Eq. (4.4)] and electron impact excitation [Eq. (4.5)],

$$O + O_2(^1\Sigma) \rightarrow O + O_2(^1\Delta), \tag{4.4}$$

$$e + O_2(^1\Delta) \rightarrow O_2(^1\Sigma) + e. \tag{4.5}$$

At the equilibrium $O_2(^1\Sigma)$ density, the sink and source terms must balance,

$$\frac{d[O_2(^1\Sigma)]}{dt} = -k_{4.4}[O][O_2(^1\Sigma)] + k_{4.5}[e][O_2(^1\Delta)] = 0, \tag{4.6}$$

where $k_{4.4}$ and $k_{4.5}$ are the rate constants for the reactions in Eqs. (4.4) and (4.5). Assuming that at high $O_2(^1\Delta)$ yields, the O and $O_2(^1\Delta)$ densities scale with the ideal gas law and that the electron density is independent of the gas density, we then obtain for the equilibrium,

$$\frac{[O_2(^1\Sigma)]}{[O_2(^1\Delta)]} = \alpha \frac{k_{4.5}[e]}{k_{4.4}\left(P/k_B T_g\right)}, \tag{4.7}$$

where α is a constant of proportionality and $(P/k_B T_g)$ is the ideal gas density. Since n_e is roughly constant, $k_{4.4}$ is proportional to $T_g^{1/2}$, and $k_{4.5}$ is a function of E/N, the ratio of densities should be inversely proportional to P and a weak function of T_g. $[O_2(^1\Sigma)]/[O_2(^1\Delta)]$ is shown in Fig. 4.7 for $\overline{E}_{dep}$ = 8 eV/molecule for a wide range of O_2 mixtures and partial pressures in He with P_{dep} = 5 W/cm^3 Torr O_2. The ratio scales with $1/P$ over a broad range of conditions, asymptotically

approaching a ratio of 0.2 at high pressure, which suggests that other processes become important at higher pressures. This is expected due to the decreasing importance of O atom quenching of $O_2(^1\Sigma)$ at higher pressures.

To demonstrate this trend, the fraction of total excitation in $O_2(^1\Delta)$,

$$f = \frac{[O_2(^1\Delta)]}{[O_2(^1\Delta)] + [O_2(^1\Sigma)]}, \tag{4.8}$$

is shown in Fig. 4.6(b) as a function of O_2 fraction and $\overline{E}_d$ (same conditions as in Fig. 4.3). There is a 25% increase in the fraction of $O_2(^1\Delta)$ as He dilution increases, corresponding to the 25% increase in raw $O_2(^1\Delta)$ yield shown in Fig. 4.3. This improvement in $O_2(^1\Delta)$ yield with He addition can be attributed to the decrease in temperature and corresponding rise in density, shifting the ratio of $O_2(^1\Sigma)$ and $O_2(^1\Delta)$ towards a lower value. This is the primary mechanism causing the scatter in yield shown in Fig. 4.2. As will be discussed below, the improved $O_2(^1\Delta)$ yields at constant $\overline{E}_d$ that result from increasing the total discharge pressure and reducing the power deposition can also be attributed to a shift in the fraction f [Eq. (4.8)].

The effect of power deposition P_d on $O_2(^1\Delta)$ yield at constant $\overline{E}_d$ and O_2 partial pressure is shown in Fig. 4.8(a). Peak $O_2(^1\Delta)$ yields are obtained at relatively low power depositions ≤1 W/cm^3. In simulations of discharges with P_d < 0.3 W/cm^3 the electron density did not consistently avalanche, and thus the discharge could not self-sustain. As P_d increases from 0.6 W/cm^3 (peak yield) to 30 W/cm^3 the yield roughly halves and is nearly independent of He addition. However, varying P_d has a smaller effect on the effective yield Y', as shown in Fig. 4.8(b). Although the peak still occurs at relatively low power depositions, Y' decreases just 5%

when P_d is increased to 30 W/cm^3. The cause for this result, as shown in Fig. 4.8(c), is that the fraction f of excited $O_2(^1\Delta)$ roughly halves when P_d is increased from 0.6 to 30 W/cm^3, which largely replicates the same trend as for the $O_2(^1\Delta)$ yield. Therefore, as with He addition, the increase in $O_2(^1\Delta)$ yield as P_d decreases is primarily caused not by a change in E/N, but by a shift in the $O_2(^1\Sigma)$ disposition in favor of $O_2(^1\Delta)$. Operation at lower power depositions requires longer discharge lengths (longer residence times) to reach the $\overline{E}_d$ at which peak yield is obtained (5-8 eV/molecule), allowing for more efficient heat transfer. This leads to lower gas temperatures and higher species densities, reducing the $[O_2(^1\Sigma)]/[O_2(^1\Delta)]$ ratio and increasing the $O_2(^1\Delta)$ yield.

Discharge operation at the lower power depositions at which $O_2(^1\Delta)$ yields are optimized requires longer discharge lengths than are typically used in COIL experiments. The power deposition selected for the discharge is ultimately a function of the desired $O_2(^1\Delta)$ yield Y and the gas flow rate. To optimize the $O_2(^1\Delta)$ yield, $\overline{E}_d$ should be 5-8 eV/molecule. For a typical discharge in a $He/O_2 = 90/10$ mixture at 30 Torr flowing at 3000 cm/s the residence time in the 30 cm discharge region is 10 ms. Thus, 500-800 eV/s-molecule must be deposited into O_2 species, corresponding to 8-12 W/cm^3 at an O_2 partial pressure of 3 Torr. This value of P_d is well above that which optimizes $O_2(^1\Delta)$ yield, as shown in Fig. 4.8(a). For comparable $\overline{E}_d$ at low power depositions, a much longer discharge is required. For example, for P_d = 0.6 W/cm^3 (in the peak $O_2(^1\Delta)$ yield zone) the discharge length would need to be 4-6 m to reach $\overline{E}_d$ = 5-8 eV/molecule – an order of magnitude longer than the 10-30 cm discharge lengths of current experiments [4-6].

When the specific energy deposition $\overline{E}_d$ and the power deposition P_d are optimized and the discharge is operating near peak yield, varying the total pressure has little effect on the $O_2(^1\Delta)$ yield. $O_2(^1\Delta)$ yield Y is shown as a function of the total pressure and O_2 mole fraction in Fig. 4.9(a) for $\overline{E}_d$ = 8 eV and P_d = 1 W/cm^3 Torr O_2. For moderate total pressures above 20 Torr, the $O_2(^1\Delta)$ yield is nearly independent of pressure. The effective yield Y' is also nearly independent of pressure above 20 Torr, as shown in Fig. 4.9(b). The small dependence of Y' on pressure is due to the already small $[O_2(^1\Sigma)]/[O_2(^1\Delta)]$ ratio for these conditions. Near the peak values ($Y \approx 0.31$, $Y' \approx 0.35$), the $[O_2(^1\Sigma)]/[O_2(^1\Delta)]$ ratio is ≈ 0.13.

To summarize the secondary effects of He addition, power deposition, and pressure, the effective yield Y' is shown in Fig. 4.10 for the same full factorial experiment of Fig. 4.2. The raw $O_2(^1\Delta)$ yield has >50% variation at a given $\overline{E}_d$ near its peak value (5-8 eV/molecule), but the effective yield ($O_2(^1\Delta)$ + $O_2(^1\Sigma)$) has <20% variation at the same $\overline{E}_d$. Since most of the $O_2(^1\Sigma)$ generated in the discharge is converted to $O_2(^1\Delta)$ in the near afterglow, Y' is likely a better indicator for COIL discharge performance. In this regard, $O_2(^1\Delta)$ production for typical flowing COIL conditions is almost exclusively a function of specific energy deposition into the oxygen species, and is nearly independent of He addition, power deposition, and pressure if enough energy (5-8 eV/molecule) is deposited.

4.6 Kinetics Sensitivity Analysis

In the context of the effective yield Y' the reaction mechanism can be conceptually simplified to five classes of processes which either generate or deplete $O_2(^1\Delta)$ and $O_2(^1\Sigma)$. The classes of production reactions are direct electron impact from the ground state and excitation

transfer from $O(^1D)$. The classes of loss processes are quenching by collisions with molecules, superelastic electron collisions and electron impact dissociation. The fractional contributions of these processes for a discharge in pure O_2 are shown in Fig 4.11(a) as a function of energy deposition.

As $\overline{E}_d$ increases, dissociation becomes more important. O atoms generated by dissociation are excited to $O(^1D)$ through electron impact [Eq. (4.9)] and then excite ground-state O_2 to $O_2(^1\Sigma)$ [Eq. (4.10)]. Excitation transfer from $O(^1D)$ becomes the most important source of $O_2(^1\Delta)$ and $O_2(^1\Sigma)$ at higher $\overline{E}_d$. Electron impact excitation of ground-state O_2 decreases as $\overline{E}_d$ increases and O_2 is depleted [Eqs. (3.1), (3.3)]. Superelastic electron impact and molecular quenching reactions are secondary loss mechanisms, making up less than 40% of the losses at $\overline{E}_d \geq 1$ eV/molecule.

The sensitivity of results from the model to the values of rate coefficients for the reactions in Table I was determined by individually varying the rate coefficients in a sensitivity analysis. When the individual rate coefficients were changed by ±10%, only four reactions caused variation ≥1% in Y'. These four reactions are the primary reactions influencing the effective yield in high yield discharges and are repeated here in order of decreasing model sensitivity:

$$e + O \rightarrow O(^1D) + e, \tag{4.9}$$

$$O(^1D) + O_2 \rightarrow O + O_2(^1\Sigma), \tag{4.10}$$

$$e + O_2 \rightarrow O_2(^1\Delta) + e, \tag{4.11}$$

$$O(^1D) + O \rightarrow O + O. \tag{4.12}$$

A full factorial sensitivity analysis showed that the 2-, 3-, and 4-way interactions between variations in the rate coefficients of these four reactions were insignificant compared to their individual (first order) effects. The sensitivity of Y' to individual variations in these four reaction rate coefficients is +10%, +7%, +5%, and –5%. For example, increasing the most sensitive rate coefficient, $k_{4.9}$ [Eq. (4.9)], by +10% changes the effective yield Y' by only +1%.

Predicted yields obtained by varying $k_{4.9}$ ±10% from its default value are shown in Fig. 4.11(b). Even at $\overline{E}_d$ = 8 eV/molecule, the effective yield is relatively insensitive to reasonable uncertainties in $k_{4.9}$. Y' ranged from 31-33%, when $k_{4.9}$ was varied ±10%. It is therefore unlikely that reasonable uncertainties in the rate coefficients will significantly change our qualitative conclusions however there may be systematic quantitative changes. It is important to note that there are physical phenomena that are not captured by the pseudo plug-flow model which may limit the optimum yields predicted here. Some of these processes are axial diffusive transport of mass and energy and other discharge instabilities such as constriction and striations.

4.7 Concluding Remarks

The gas phase kinetics of flowing He/O_2 discharges used in COIL systems have been investigated. Using a modified global plasma kinetics model to simulate the plug flow, the effects of velocity, pressure, power deposition, and He addition on the $O_2(^1\Delta)$ yield were investigated. The $O_2(^1\Delta)$ yield was found to scale principally with specific energy deposition into oxygen species. Increasing the specific energy deposition increases the $O_2(^1\Delta)$ yield up to a peak value of ≈0.3 near $\overline{E}_d$ = 5-8 eV/molecule. At a constant specific energy deposition near peak yield, adding He, reducing the power deposition, and increasing the pressure increases the

$O_2(^1\Delta)$ yield to lesser extent than specific energy deposition. Although these secondary effects increase $O_2(^1\Delta)$ yield in the discharge, they have little effect on the combined $O_2(^1\Delta)$ and $O_2(^1\Sigma)$ yield. Since most of the $O_2(^1\Sigma)$ is converted to $O_2(^1\Delta)$ in the early afterglow, the discharge performance for COIL systems will likely be determined by specific energy deposition.

4.8 Figures

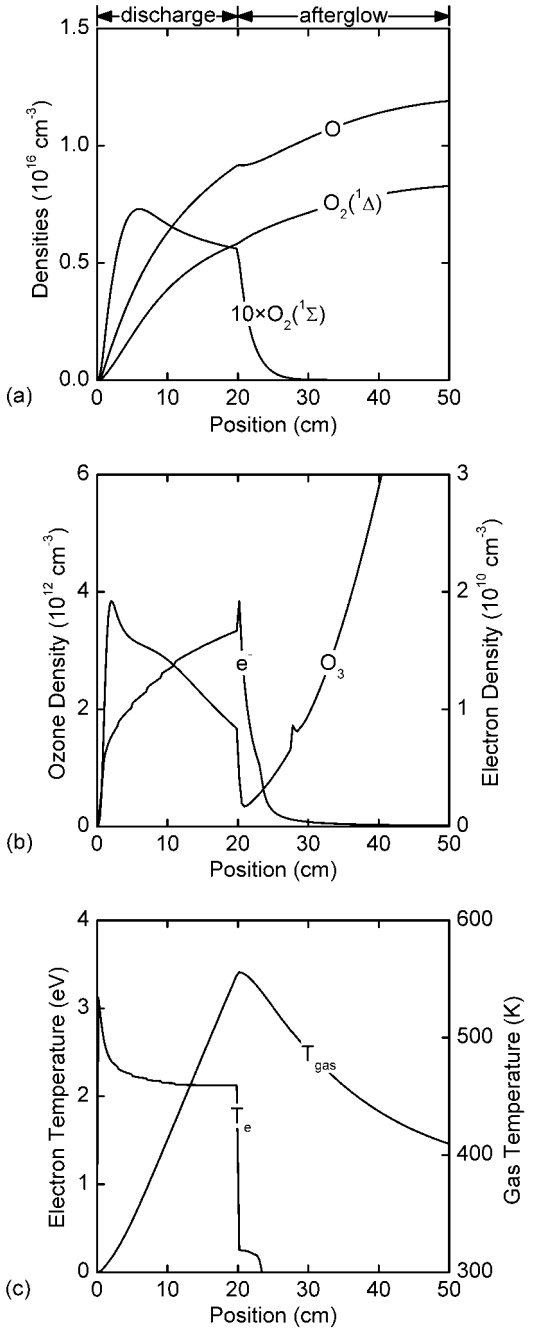

Fig. 4.1. Plasma properties for the base case (O_2 at 3 Torr: L = 20 cm, $v_{x,in}$ = 1000 cm/s, P_d = 0.5 W/cm^3). (a) $O_2(^1\Delta)$, $O_2(^1\Sigma)$, and O atom densities. (b) O_3 and electron densities. (c) Electron and gas temperatures.

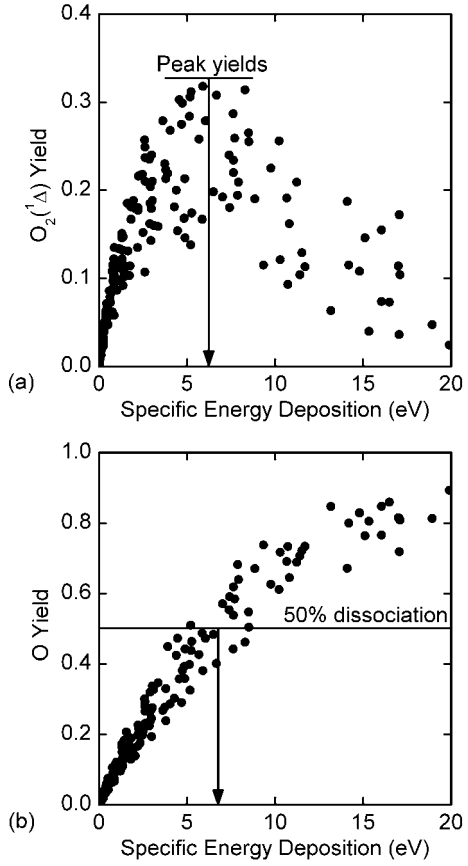

Fig. 4.2. Yields for a 4 level full factorial design-of-experiments for a 20 cm discharge. (a) $O_2(^1\Delta)$ yields. (b) O yields. The peak $O_2(^1\Delta)$ yield reaches ≈0.3 as dissociation reaches 0.5 at $\overline{E}_d$ = 5-8 eV/molecule.

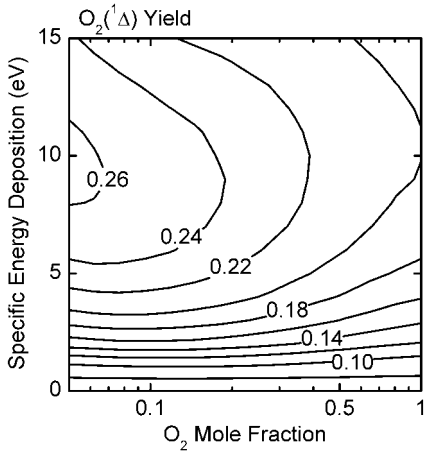

Fig. 4.3. $O_2(^1\Delta)$ yield as a function of O_2 mole fraction (balance He) and specific energy deposition into O_2 for a constant partial pressure of O_2 of 4.2 Torr. P_d = 21 W/cm^3, $v_{x,in}$ = 2500 cm/s, and length was varied to obtain the specific energy depositions. The $O_2(^1\Delta)$ yield increases as He is added for parameters near the peak yield ($\overline{E}_d$ = 5-8 eV).

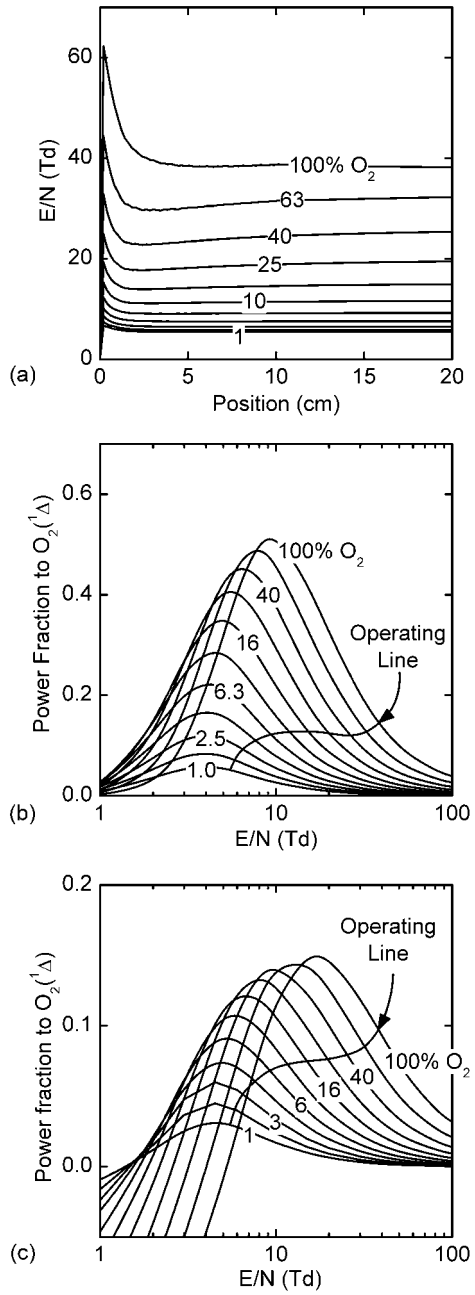

Fig. 4.4. Effect of diluent on discharge electrodynamics for mixtures of 1-100% O_2 in He at 3 Torr O_2 partial pressure. (a) E/N for various mixtures as a function of discharge length. (b) Fraction of electron power exciting O_2 to $O_2(^1\Delta)$ as a function of E/N at 0% yield, and (c) 15% yield. The operating line shows where the quasi-steady discharge sustains for each mixture. Electron power spent exciting $O_2(^1\Delta)$ decreases as He addition increases.

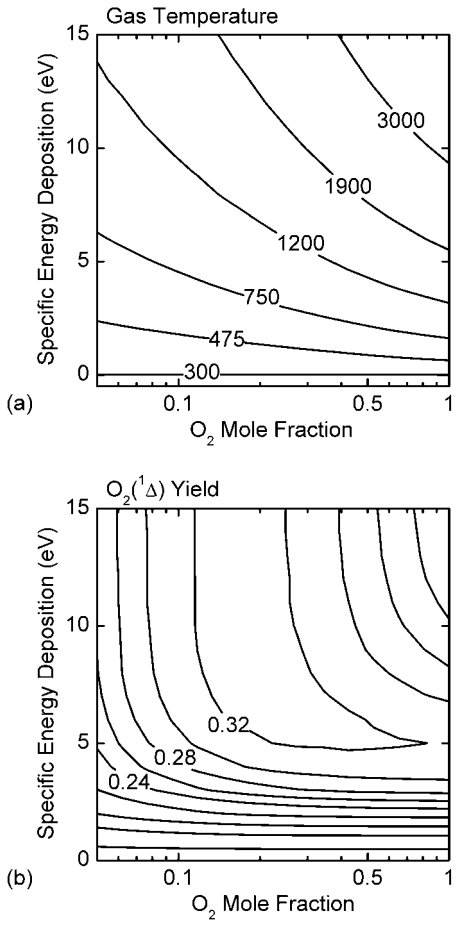

Fig. 4.5. Effect of He dilution on gas heating. (a) T_g as a function of specific energy deposition and mixture, showing a decrease in gas temperature when O_2 is diluted to 5%. (b) $O_2(^1\Delta)$ yield as a function of O_2 mole fraction and specific energy deposition. The conditions are the same as Fig. 4.3, except that T_g is fixed at 300 K. The dependence of $O_2(^1\Delta)$ yield on He addition is less pronounced when there is no gas heating.

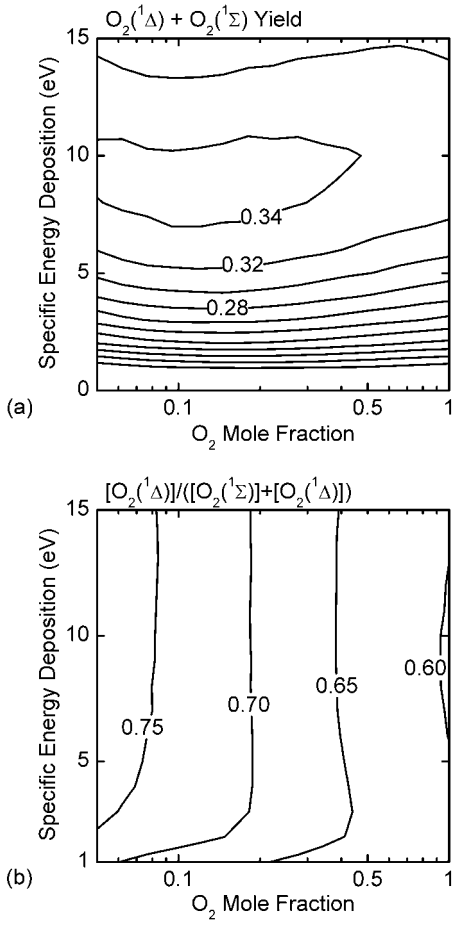

Fig. 4.6. Effect of $[O_2(^1\Sigma)]/[O_2(^1\Delta)]$ partition on $O_2(^1\Delta)$ yield. (a) Effective yield Y' of $O_2(^1\Sigma)$ + $O_2(^1\Delta)$ as a function of specific energy deposition and mixture. (b) f = $[O_2(^1\Delta)]/([O_2(^1\Delta)]+[O_2(^1\Sigma)])$ as a function of specific energy deposition and mixture. Conditions are the same as in Fig. 4.3. The fraction of $O_2(^1\Delta)$ increases as He is added to the discharge, causing the $O_2(^1\Delta)$ yield to increase, but the effective yield Y' is relatively unaffected.

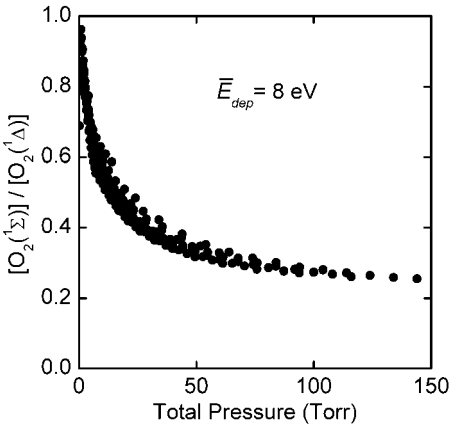

Fig. 4.7. $[O_2(^1\Sigma)]/[O_2(^1\Delta)]$ as a function of pressure for $\overline{E}_{dep}$ = 8 eV/molecule. O_2 mole fractions range from 0.05 to 1.0 in He with O_2 partial pressures from 0.2 to 7.2 Torr. P_d is 5 W/cm^3 Torr O_2. $[O_2(^1\Sigma)]/[O_2(^1\Delta)]$ is inversely proportional to pressure except at low ratios, where other $O_2(^1\Sigma)$ reactions become important.

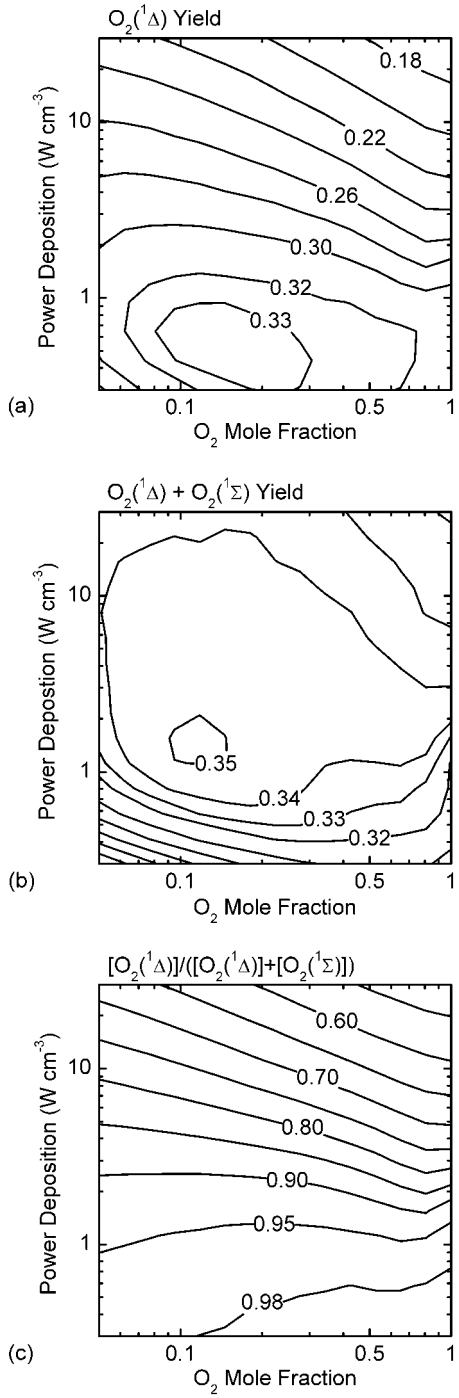

Fig. 4.8. Yields as a function of power deposition and O_2 mole fraction for $\overline{E}_d$ = 8 eV/molecule and O_2 partial pressure of 3 Torr. (a) $O_2(^1\Delta)$ yield Y. (b) $O_2(^1\Delta)$ and $O_2(^1\Sigma)$ combined yield Y'. (c) $O_2(^1\Delta)$ fraction f. $O_2(^1\Delta)$ yield and fraction are higher at low P_d because more $O_2(^1\Sigma)$ has been converted to $O_2(^1\Delta)$, but the combined yield is relatively constant from 1-10 W/cm^3.

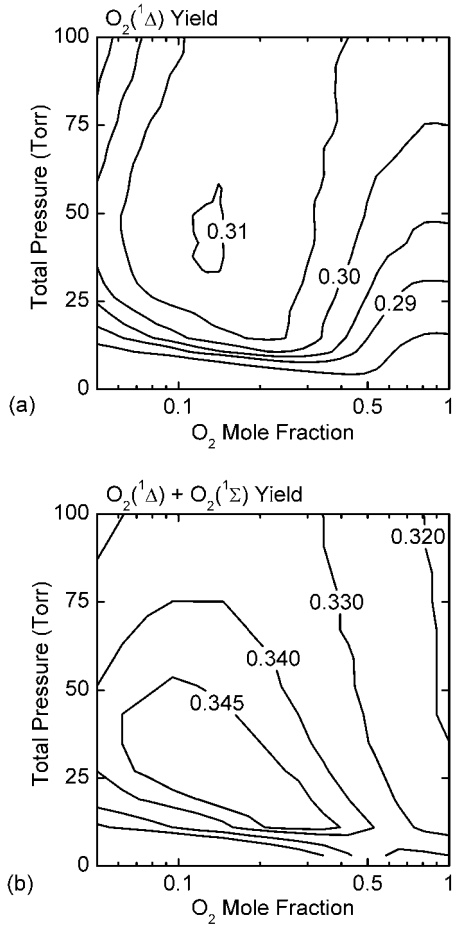

Fig. 4.9. $O_2(^1\Delta)$ yields at $\overline{E}_d$ = 8 eV/molecule as a function of total pressure and O_2 mole fraction at a P_d of 3 W/cm^3 Torr O_2. (a) $O_2(^1\Delta)$ yield Y. (b) $O_2(^1\Delta)$ and $O_2(^1\Sigma)$ combined yield Y'. When $\overline{E}_d$ and P_d have been optimized, neither Y nor Y' are strong functions of total pressure above 20 Torr.

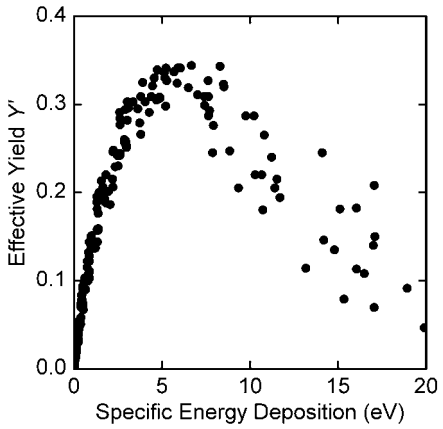

Fig. 4.10. Effective yield Y' for same conditions as Fig. 4.3. At fixed $\overline{E}_d$ in the peak effective yield regime (5-8 eV/molecule), there is less scatter than for the $O_2(^1\Delta)$ yield Y [Fig. 4.2(a)].

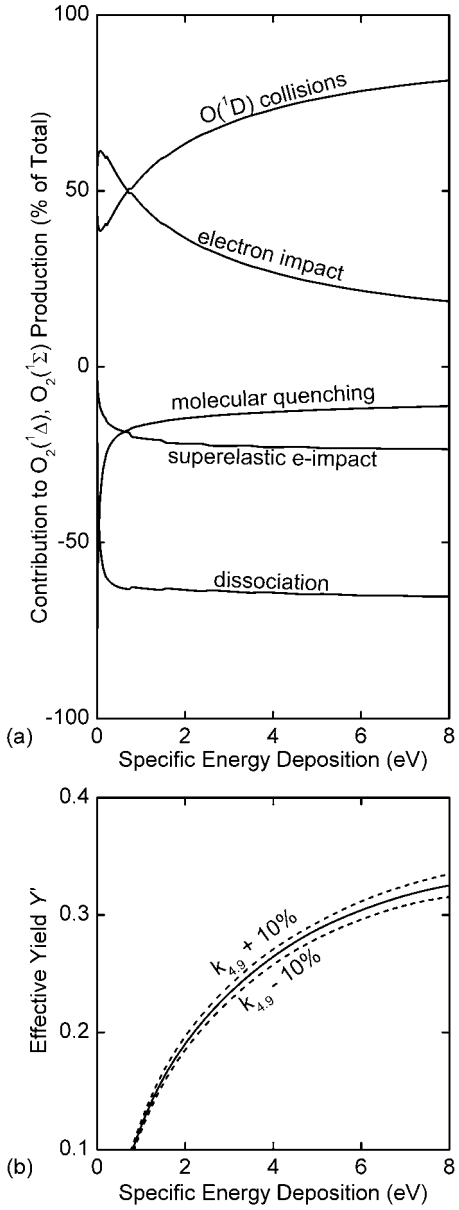

Fig. 4.11. Importance of classes of reactions as a function of specific energy deposition $\overline{E}_d$ in pure O_2. (a) $O_2(^1\Delta)$ and $O_2(^1\Sigma)$ production or loss processes as a percentage of the total production rate. (b) Sensitivity of the effective yield Y' to ±10% uncertainty in $k_{4.9}$. Conditions are the same as in Fig. 4.3. As $\overline{E}_d$ increases later in the discharge, $O(^1D)$ collisions dominate $O_2(^1\Delta)$ production. At $\overline{E}_d$ = 8 eV/molecule, $O(^1D)$ reactions also account for most of the sensitivity in the model, where ±10% variation in $k_{4.9}$ causes ±1% variation in Y'.

4.9 References

1. King, D.M., et al. *ElectriCOIL: Preliminary Experiments of Excited Oxygen Generation by RF Discharge*. in *Proceedings of the International Conference on Lasers*. 2000. Albuquerque, NM: STS Press, McLean, VA, 2001.
2. Napartovich, A.P., A. Deryugin, and I. Kochetov, *Discharge production of the singlet delta oxygen for an iodine laser.* Journal of Physics D: Applied Physics, 2001. 34: p. 1827-1833.
3. Carroll, D.L., et al., *Recent Experimental Measurements of the ElectriCOIL System.* AIAA Paper 2003-4029, 2003.
4. Rakhimova, T.V., et al., *Radio-frequency plasma generation of singlet oxygen in O_2 and O_2:Ar(He) mixtures.* AIAA Paper 2003-4306, 2003.
5. Savin, Y.V., et al., *Traveling microwave discharge as a singlet delta oxygen source.* AIAA Paper 2003-4305, 2003.
6. Carroll, D.L., et al., *Recent Electrodynamics Modeling of the ElectriCOIL System.* AIAA Paper 2003-4030, 2003.

5. CONSEQUENCES OF AXIAL TRANSPORT ON $O_2(^1\Delta)$ YIELD

5.1 Introduction

The one-dimensional model was used to investigate the effects of axial transport of mass, momentum, and energy on the yield of $O_2(^1\Delta)$. In particular, experimental results show that the plasma zone propagates significantly both upstream and downstream of the electrodes in a capacitive coupled plasma (CCP) or the coils in an inductive coupled plasma (ICP) [1, 2]. This effect cannot be captured with the global kinetic model or from first principles with the specified power deposition used in the 1-D model. As a result, 1-D simulations were performed with the same kinetic mechanism discussed in Chapter 3 using more detailed power deposition models. Since the one-dimensional simulations are much more computationally intensive than the global simulations, a significantly smaller parameter space was investigated. The parameter space was chosen so that the results would be relevant to current experiments being performed on electric discharge COIL's. Thus, the $O_2(^1\Delta)$ yields and specific energy depositions investigated with the 1-D model are more modest, on the order of 0.15 and 1 – 3 eV/molecule, respectively. Results for a base case one-dimensional simulation in this parameter space will be described in Section 5.2, followed by a discussion of the specific energy deposition scaling in Section 5.3 and a discussion of advective effects in Section 5.4.

To first order, the $O_2(^1\Delta)$ yield obtained with the one-dimensional model was found to scale with specific energy deposition into O_2 species as was predicted by the global model. Also as predicted by the global model, the effects of diluting with He was found to have a smaller, second order effect on the $O_2(^1\Delta)$ yield compared to the specific energy deposition, as will be shown in Section 5.5. Results from the two power deposition models, CCP and ICP, are

compared in Section 5.6. These new power deposition models facilitated modeling of pulsed discharges. Pulsed discharges were found to provide significant increases in $O_2(^1\Delta)$ yield at a given specific energy deposition, as will be discussed in Section 5.7. A discharge instability that was observed under some conditions will be described in Section 5.8. Concluding remarks are in Section 5.9.

5.2 Typical Discharge Behavior

The base case uses conditions similar to experiments performed by Carroll, *et al.*, which achieved positive gain in an electric discharge COIL system [3]. The discharge tube is the same as described in Section 4.2, with capacitive electrodes on the discharge tube outer diameter spaced 20 cm apart. The driven electrode is upstream of the ground electrode. The total pressure is 10.6 Torr, with an 80/20 mixture of He/O_2 fed into the discharge at 20 mmol/s. This flow rate corresponds to an axial velocity of $\approx$2000 cm/s into the discharge region. The absorbed power in the base case is 340 W at 13.56 MHz. The capacitances required for the CCP transmission line parameters [Fig. 2.2] were calculated based on geometry, assuming an infinitely long coaxial capacitor (the discharge tube) suspended above a 15 cm wide ground plane 15 cm below the discharge tube. This configuration in conjunction with the geometry and material properties of the Pyrex discharge tube yields capacitances on the order of 100 pF/cm. The capacitance at the external electrodes is larger by a factor of 100.

Densities of $O_2(^1\Delta)$, $O_2(^1\Sigma)$, O, and O_3 for the base case, one-dimensional simulation are shown in Fig. 5.1(a) for the CCP model. The axial length of the computational domain is 150 cm, with the upstream (driven) electrode being 50 cm from the inlet, and the downstream (ground) electrode being 70 cm from the inlet. The results shown in Fig. 5.1 correspond to the

steady state. (Although the one-dimensional model is time dynamic, only steady-state results will be discussed here.) Comparing these results to those of the global model base case [Fig. 4.1], we see that the species densities at the end of the discharge region are roughly the same for both simulations. The O atom density has again exceeded the $O_2(^1\Delta)$ density, and the $O_2(^1\Sigma)$ density decreases rapidly in the afterglow. In addition, O_3 does not begin to play an important role until the afterglow, several tens of cm downstream of the discharge region. However, we see that the most significant difference between the global and one-dimensional models is that the species densities in Fig. 5.1(a) begin to increase far upstream (≈20 cm) of the driven electrode. This is partly due to the axial transport of the plasma and partly due to the CCP power deposition model.

The extent of the plasma zone is shown more clearly in Fig. 5.1(b) by the electron density profile. The electron density reaches 10^9 cm^{-3} by 20 cm upstream of the driven electrode because of upstream transport (diffusion) of electrons and subsequent ionization. The relatively steep rise in electron density at this point marks the front end of the reactive plasma zone. Power deposition (and energy deposition) becomes important by this position, and electron impact processes with O_2 begin to dominate the kinetics. The electron temperature spikes upstream of this point, due to the electron density avalanching process described in Section 4.2. However, the spike is not as large as that shown in Fig. 4.1(c) because of there being axial transport of electrons upstream of the main plasma zone. The presence of electrons in the upstream region also increases the axial conductivity of the plasma, facilitating power deposition in this region by capacitive coupling. The same action occurs on the downstream side of the discharge, increasing the length of the afterglow. The asymmetry of the electron density is due in part to downstream advection and in part to dissociation of the O_2 that produces a more readily ionized gas mixture.

5.3 Input Power and Yield Scaling

The effect of increasing the CCP power while fixing the other conditions is shown in Fig. 5.2. The average electron density in the bulk plasma zone increases roughly linearly with input power [Fig. 5.2(a)]. The plasma zone can also be seen to extend slightly upstream and downstream of the electrodes as the power is increased. As mentioned above, this effect is caused by higher axial conductivity in the plasma allowing the capacitive coupling to reach further away from the region between the electrodes.

When the input powers are converted to specific energy depositions, the peak $O_2(^1\Delta)$ yield scales with specific energy deposition to first order, as shown in Fig. 5.2(b). These results closely parallel those obtained with the global model for peak $O_2(^1\Delta)$ yields [as shown in Fig. 4.2(a)], albeit over a smaller parameter space of up to 3 eV/molecule deposited into O_2 equivalent species. The peak gas temperature also increases rapidly with specific energy deposition, reaching almost 800 K by 3 eV/molecule. The O atom density as a function of specific energy deposition, shown in Fig. 5.2(c), increases at a larger rate than the $O_2(^1\Delta)$ density as specific energy deposition is increased. These results are similar to those for the global model [see Fig. 4.2(b)]. Therefore, to first order, the scaling based on the global plasma kinetic modeling discussed in Chapter 4 holds when axial transport and capacitive power deposition are considered.

5.4 Advection

The effect of increasing the inlet flow rate is shown in Fig. 5.3, where power has also been increased so that the overall specific energy deposition remains constant. As the power increases the electron density increases by roughly the same factor, as shown in Fig. 5.3(a). It is

also apparent from the electron density profile that the afterglow region expands further downstream at higher flow velocities. Although the expansion of the plasma zone can be partially attributed to the increase in power, there is an additional flow-induced expansion of the plasma zone [compare Fig. 5.3(a) to Fig. 5.2(a)]. The expansion induced by the flow has little effect on the electron temperature, as shown in Fig. 5.3(b). Consequently, the electron impact reaction rate coefficients do not change significantly. Although the location of the peak $O_2(^1\Delta)$ yield is shifted downstream by the increasing velocity, the absolute value is close to the base case value [Fig. 5.3(c)] since the specific energy deposition is held constant.

The flow-induced expansion is readily apparent when the power is kept constant while the inlet velocity is increased, as shown in Fig. 5.4(a). Here, the bulk electron density in the discharge decreases approximately linearly with specific power deposition. However, even though the bulk electron density decreases with increasing flow, the plasma zone is extended at larger velocities so that the electron density increases tens of cm downstream of the electrodes. This flow-induced expansion of the plasma is due to momentum transfer from the bulk fluid to the ions. As the flow rate increases and residence time in the plasma decreases, the specific energy deposition also decreases. As such, there is less dissociation and less excitation, resulting in a more attaching gas mixture (lower electron density) and lower $O_2(^1\Delta)$ yield, as shown in Fig. 5.4(b).

5.5 He Dilution

In Section 4.4, the addition of He diluent was shown to have a small secondary effect on $O_2(^1\Delta)$ yield. In particular, the addition of He was shown to increase the $[O_2(^1\Delta)]/[O_2(^1\Sigma)]$ ratio in the discharge, while only weakly affecting the total $O_2(^1\Delta)+O_2(^1\Sigma)$ density [Fig. 4.6(a)]. He

addition also has a weak influence in the one-dimensional model, with the net effect being that the $O_2(^1\Delta)$ yield decreases as He is added, as shown in Fig. 5.5(a). The large thermal conductivity of He/O_2 mixtures also results in similar gas temperatures for the various mixtures one meter downstream of the discharge [Fig. 5.5(b)]. In terms of efficiency of $O_2(^1\Delta)$ production, where efficiency is defined as [$O_2(^1\Delta)$ yield]/[$\overline{E}_d$], the addition of He also has little effect. When the He content is increased from 50% to 85%, the efficiency of $O_2(^1\Delta)$ production changes by only a few percent, as shown in Fig. 5.5(c). Therefore, as predicted by the global model, the effect of He addition is much weaker than the first order scaling with $\overline{E}_d$.

5.6 ICP vs. CCP Power Deposition

Although most current electric discharge COIL experiments use capacitive or microwave power, inductive coupling has previously been investigated for $O_2(^1\Delta)$ generation [2]. The ICP model used in the one-dimensional simulation assumes pure inductive coupling and was described in Section 2.4. A comparison of the results using pure inductive and pure capacitive discharge models is shown in Fig. 5.6. The inductive coupling is provided by 21 evenly spaced coils wound on the discharge tube OD from 50 to 70 cm and the capacitive coupling is provided as in the base case. The power for both cases is 340 W.

The $O_2(^1\Delta)$ yield obtained in the CCP simulation is slightly larger than that obtained with the ICP model, as shown in Fig. 5.6(c). This occurs even though the peak electron density is larger for the ICP model. This disparity results from the electron temperature for the bulk plasma being higher for the ICP case than for the CCP case, shown in Fig. 5.6(a,b). Thus, the bulk of the electrons in the CCP case are at a lower temperature than the bulk of the electrons in the ICP case. The rate of $O_2(^1\Delta)$ production by electron impact is more favorable at the lower

electron temperature in the CCP, thereby producing slightly larger $O_2(^1\Delta)$ yields. The importance of the average electron temperature in the discharge will be discussed in Section 5.6.

Interestingly, the electron density in the inductive discharge appears to be pushed to the end of the coil solenoid [Fig. 5.6(a)]. Not shown is the dynamic result where the plasma originates symmetrically in the solenoid, but is pushed to the downstream end as the simulation approaches the steady-state. Investigations in pure He have shown that this effect does not occur in an isothermal gas, and is actually caused by a feedback mechanism between the ICP power deposition and rarification of the gas in discharge. It is clear that this feedback is supported by the strong $1/r_{ij}^3$ dependence of the axial magnetic field from any given coil. However, it is not clear that this is a physically plausible result.

5.7 Pulsed Power Deposition

Much of the current research in development of electric discharge COIL's has focused on engineering the operating *E/N* of the discharge to be closer to the optimal value for $O_2(^1\Delta)$ production. The fractions of electron power dissipated by various electron impact processes as a function of electron temperature in pure O_2 are shown in Fig. 5.7(a). It is clear that to optimize the fractional power dissipated in the electron impact production of $O_2(^1\Delta)$,

$$e + O_2 \rightarrow O_2(^1\Delta) + e\,, \tag{5.1}$$

the electron temperature should be near 1.2 eV. This electron temperature corresponds to an *E/N* of ≈10 Td. Unfortunately, self-sustained discharges in He/O_2 mixtures operate at at least a few tens of Td (see Fig. 4.4 and Section 4.4), roughly corresponding to the peak in dissociation at T_e

= 2.1 eV. Various methods have been investigated to manage the *E/N* such as increasing the number density of the gas with an inert diluent such as He [4], adding other components to reduce the ionization potential of the gas (NO, for example [5]), or by sustaining ionization via an e-beam [6].

One other interesting alternative is to use a pulsed rf discharge akin to that proposed by Hill [7], wherein a fast, high power rf pulse is followed by a long period of low "background" power, as shown in Fig. 5.7(b). The duration of the high power pulse should be just long enough for the electron temperature spike to cause a large increase in ionization by avalanching the electron density, such as is shown pictorially in Fig. 5.7(c). After the high power pulse, the background power level is applied to more moderately heat the electrons. If the excess ionization is sufficient, there will be an extended period where the electron temperature falls below the self-sustaining value, allowing optimization of T_e to produce $O_2(^1\Delta)$. The application of the peak power pulse should be short so that the average power applied over the whole pulse period remains nearly the same as the cw case.

The resulting electron temperature and density from a pulsed power scheme at quasi-steady-state are shown in Fig. 5.8, where a 2.5 kW pulse is applied for 100 ns followed by a 4 μs delay before the next pulse. Background power was applied during the delay at a level near to 340 W so as to keep the average power at 340 W. Other conditions were the same as for the base case discussed in Section 5.2. Although the electron temperature does spike during the pulse as expected, the electron density in fact *decreases* during the pulse. This is due to the strong attaching nature of the O_2 gas through the ground state and $O_2(^1\Delta)$,

$$e + O_2 \rightarrow O^- + O + e\,, \tag{5.2}$$

$$e + O_2(^1\Delta) \rightarrow O^- + O + e. \quad (5.3)$$

When the electron temperature increases during the high power pulse, roughly 10% of the electrons immediately attach through Eqs. (5.2) and (5.3) and the O^- concentration increases by the same density change. After the pulse, detachment occurs at a slower rate, causing the electron density to increase throughout the delay period. Also apparent from Fig. 5.8 is that the pulse delay could have been extended longer, i.e., the electron temperature had not yet recovered to the self-sustaining value at the end of the 4 μs delay. In fact, the electron temperature has not even begun increasing after 4 μs in Fig. 5.8. Pulsed discharge experiments by Hicks, *et al.*, suggest that the electron temperature recovery to the self-sustaining value may take over 10 μs [8]. However, the net effect of this basic pulsing scheme is the same as described above. The high power pulses allow the discharge to operate below the self-sustaining *E/N*.

The results of three modest pulsing schemes are compared to the equivalent cw discharge in Fig. 5.9. In these three schemes, the high power CCP pulse is applied at 2.5 kW for 100 ns followed by delay periods of 1, 2, and 4 μs. The background power is adjusted so that the average power is kept at 340 W. As shown in Fig. 5.9(a), the average electron temperature during the interpulse period is significantly lower than the cw electron temperature. The average temperature in the cw discharge of ≈2 eV corresponds to the peak in electron impact dissociation of O_2, while the average temperature for the 2 and 4 μs pulsed schemes is closer to 1 eV, corresponding to the peak in $O_2(^1\Delta)$ excitation [Fig. 5.7(a)]. The result is the dramatic ≈50% improvement in $O_2(^1\Delta)$ yield shown in Fig. 5.9(b). Although the background electron temperature is lower for the 1 μs delay than for the 2 and 4 μs delays, the overall fraction of time spent in the high power pulse is twice as long, causing the lower $O_2(^1\Delta)$ yield seen with the 1 μs

delay. The reduced O atom yield shown in Fig. 5.9(c) confirms for all three schemes that the discharge is no longer operating at an electron temperature favorable to O_2 dissociation. Furthermore, it appears that the $O_2(^1\Delta)$ yield available at these conditions has saturated at a 2 μs delay and that further delays do not significantly increase $O_2(^1\Delta)$ yields. This saturation effect has been confirmed with simulations of 10 and 20 μs delays which showed no further increase in $O_2(^1\Delta)$ yield over the 2 μs delay when a 100 ns pulse at 2.5 kW is applied.

The pulsed discharges were the only cases we investigated that show significant departure from the specific energy deposition scaling presented in Section 4.3. At the same $\overline{E}_d$ as the base case discussed in Section 5.2 (0.88 eV/molecule), the 2 and 4 μs delays produced almost 50% higher $O_2(^1\Delta)$ yields than the base case. With further optimization of the pulse power, duration, delay, and background power, the pulsed schemes could produce even larger yields. Pulsed schemes may also be helpful in alleviating discharge instability problems caused by gas heating and resultant rarification and discharge constriction.

5.8 Discharge Instability

An instability that was observed for select conditions using a CCP power scheme is shown in Fig. 5.10. The instability manifests itself as an upstream oscillation in electron temperature that propagates into the electron density and then into other process variables. The instability is only observed upstream of the discharge electrodes in the CCP cases and is apparently exacerbated by conditions that allow a large extent of upstream propagation of the plasma. For example, if the wall capacitances are reduced then the rf current sees a higher resistance to ground and will therefore propagate further along the axis before traveling through the discharge tube wall. This condition, using half of the calculated capacitances, is shown in

Fig. 5.10(a). Alternatively, if the conductivity along the discharge is increased, for example by increasing the power and electron density, then the rf current will also travel further upstream and downstream of the electrodes before passing through the wall capacitance. This condition is shown in Fig. 5.10(b) when the CCP power is > 1 kW, with other conditions the same as the base case.

It is not clear whether this instability is physical or is caused through feedback to the one-dimensional CCP power deposition model. For computational efficiency, a relatively coarse discretization was applied using only 60 points for the 1.5 m domain. A hyperbolic mapping allowed finer resolution in the plasma zone between the electrodes. It is plausible that this resolution is too coarse to allow the use of the transmission line model (Section 2.4) close the edges of the domain.

5.9 Concluding Remarks

The effects of axial transport and various power deposition models have been investigated with a one-dimensional axial flowing plasma kinetics model. The one-dimensional results for cw CCP and ICP discharges produced the same scaling of $O_2(^1\Delta)$ yield with specific energy deposition as the zero-dimensional model in the somewhat smaller parameter space investigated. The effect of adding He as a diluent was shown to be smaller than the contribution of specific energy deposition, as predicted by the global model. Comparing the ICP model with the CCP model revealed that CCP discharges promote slightly higher $O_2(^1\Delta)$ yields due to a more optimal (lower) electron temperature in the bulk plasma. Pulsed discharges showed the most promise for improving yields, with modest pulsing schemes achieving up to 50% higher $O_2(^1\Delta)$ yields than cw cases at the same $\overline{E}_d$ while also reducing O_2 dissociation. A discharge

instability was observed when the plasma zone propagated too far upstream, which could potentially be eliminated by the use of a finer resolution mesh.

5.10 Figures

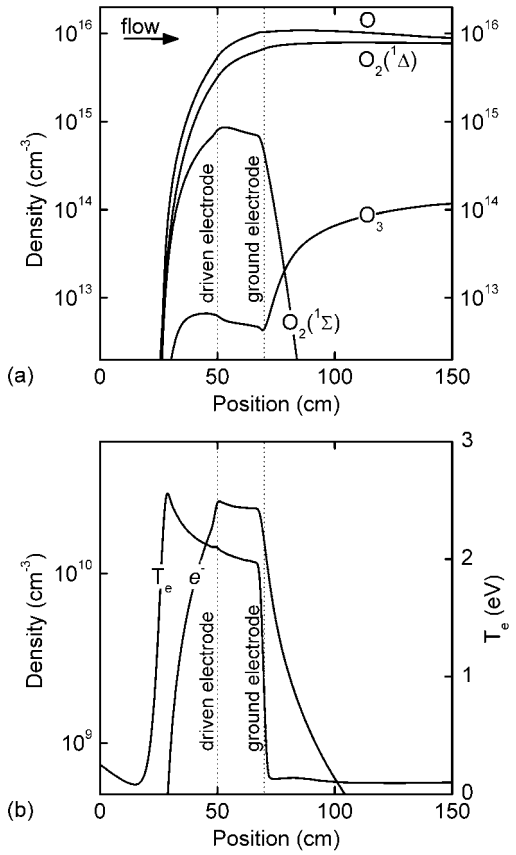

Fig. 5.1. Plasma properties for the steady-state base case. Conditions: inlet flow of 20 mmol/s He/O_2 = 80/20 at 10.6 Torr and 300 K; 340 W CCP discharge at 13.56 MHz with driven electrode at 50 cm, ground electrode at 70 cm. (a) $O_2(^1\Delta)$, $O_2(^1\Sigma)$, O atom, and O_3 densities. (b) Electron density and temperature. The inclusion of axial transport into the model demonstrates the propagation of the plasma upstream and downstream of the electrodes.

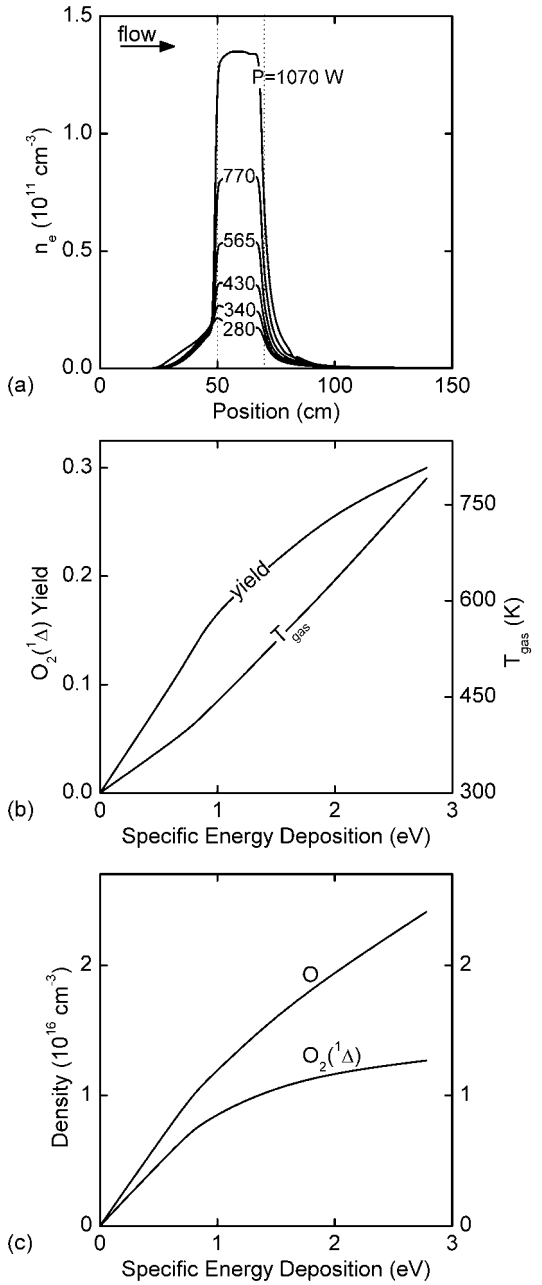

Fig. 5.2. Effect of increasing the capacitive power. Conditions are the same as for the base case (Fig. 5.1), except for power. (a) Electron densities at various powers as a function of distance along the discharge tube axis. (b) Peak $O_2(^1\Delta)$ yield and T_{gas} where power has been converted to specific energy deposition. (c) Peak $O_2(^1\Delta)$ and O atom densities as a function of specific energy deposition. As with the 0-D model, $O_2(^1\Delta)$ yield scales with specific energy deposition at these conditions.

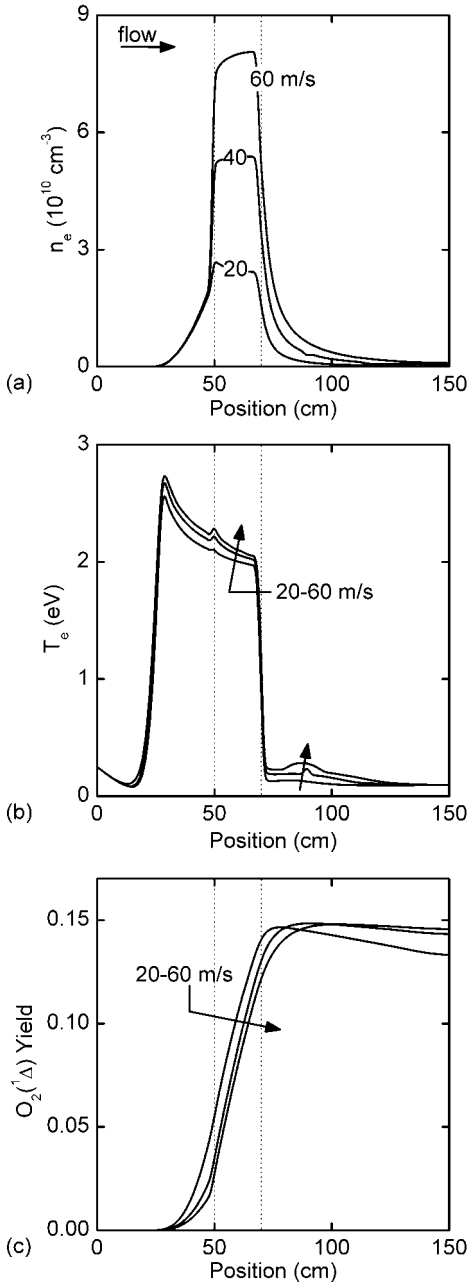

Fig. 5.3. Effect of increasing the throughput. Inlet flow rate was increased from 20 mmol/s (base case) to 40 and 60 mmol/s, which correspond to ≈20, 40, and 60 m/s inlet speeds. Power was increased from 340 W (base) to 680 and 1020 W to keep $\overline{E_d}$ constant. Other conditions are the same as for the base case (Fig. 5.1). (a) Electron density and (b) temperature at 20, 40, and 60 m/s as a function of distance along the discharge tube axis. (c) $O_2(^1\Delta)$ yield along the discharge. The increasing flow velocity causes the location of peak $O_2(^1\Delta)$ yield to move further down the discharge tube, but the value of the peak $O_2(^1\Delta)$ yield does not change.

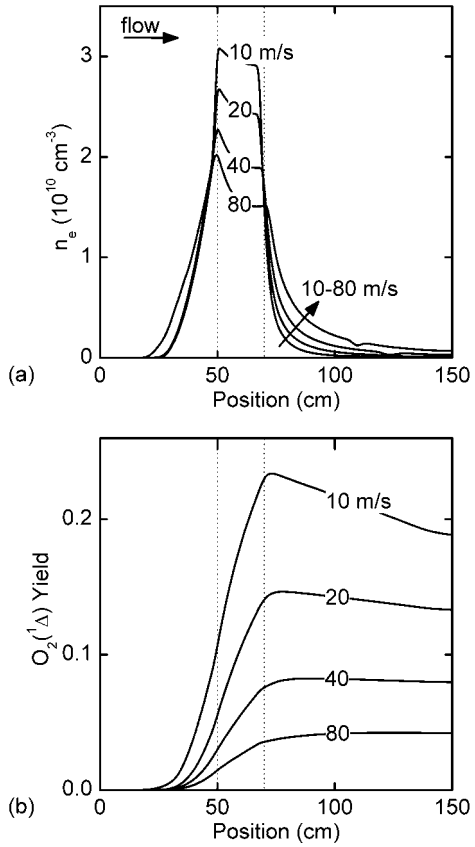

Fig. 5.4. Effect of increasing the inlet velocity. Inlet flow rate is shown at 10, 20, 40 and 80 mmol/s, which correspond to ≈10, 20, 40, and 80 m/s inlet speeds. Other conditions, including power, are the same as for the base case (Fig. 5.1). (a) Electron density and (b) $O_2(^1\Delta)$ yield along the discharge for 10, 20, 40, and 80 m/s flow rates. The increasing flow velocity causes expansion of the downstream portion of the plasma zone due to momentum transfer from the bulk fluid to the ions. $O_2(^1\Delta)$ decreases with flow rate as power is kept constant.

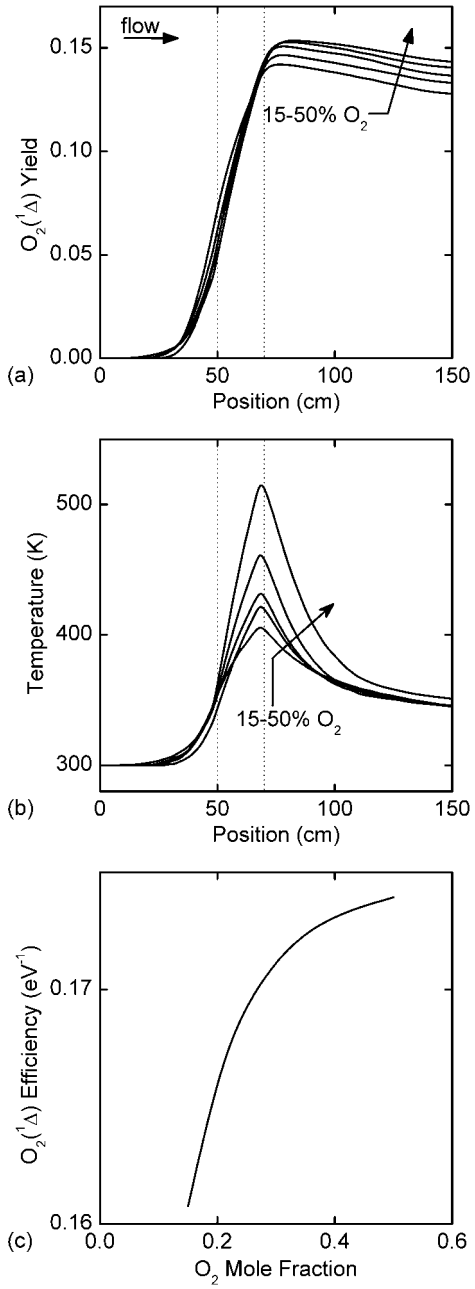

Fig. 5.5. Dilution of the O_2 flow using He. Conditions are the same as in Fig. 5.1 with the O_2 molar flow and partial pressure held constant as He is added to the flow. (a) $O_2(^1\Delta)$ yield along the discharge for 15, 20, 25, 35, and 50 % O_2 mixtures in He. (b) T_{gas} for the same mixtures as in (a). (c) Efficiency of $O_2(^1\Delta)$ production for the same mixtures. The addition of He reduces T_{gas} as expected, but decreases the efficiency of $O_2(^1\Delta)$ production at these conditions.

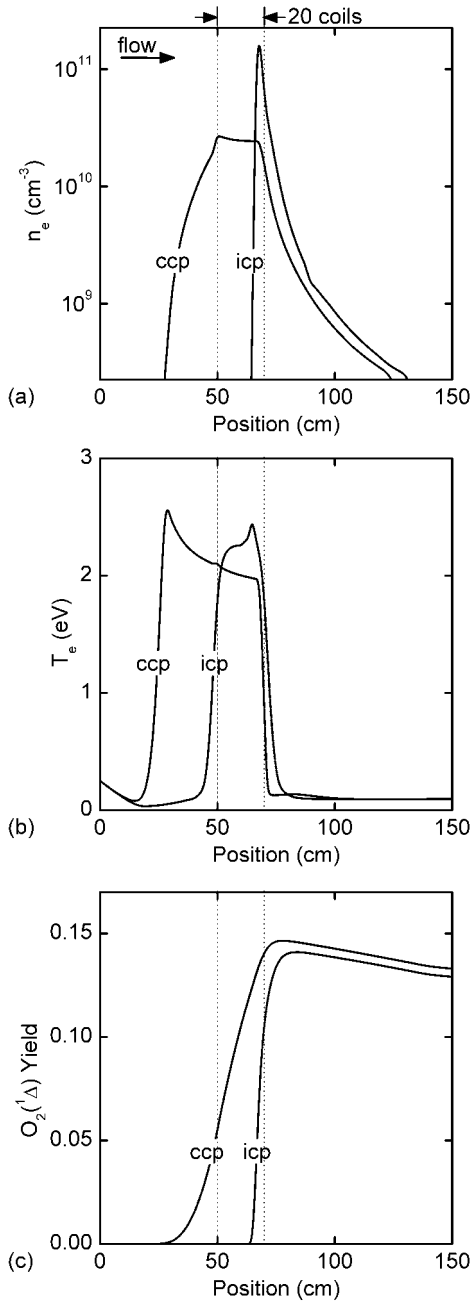

Fig. 5.6. Comparison of capacitive and inductive discharges. For the ICP case power is inductively coupled through 21 coils spaced evenly on the discharge tube from 50 to 70 cm; other conditions and the CCP case are the same as in Fig. 5.1. (a) Electron density, (b) electron temperature, and (c) $O_2(^1\Delta)$ yield along the discharge axis. The CCP case produces slightly higher $O_2(^1\Delta)$ yield than the ICP case due to lower T_e in the bulk plasma.

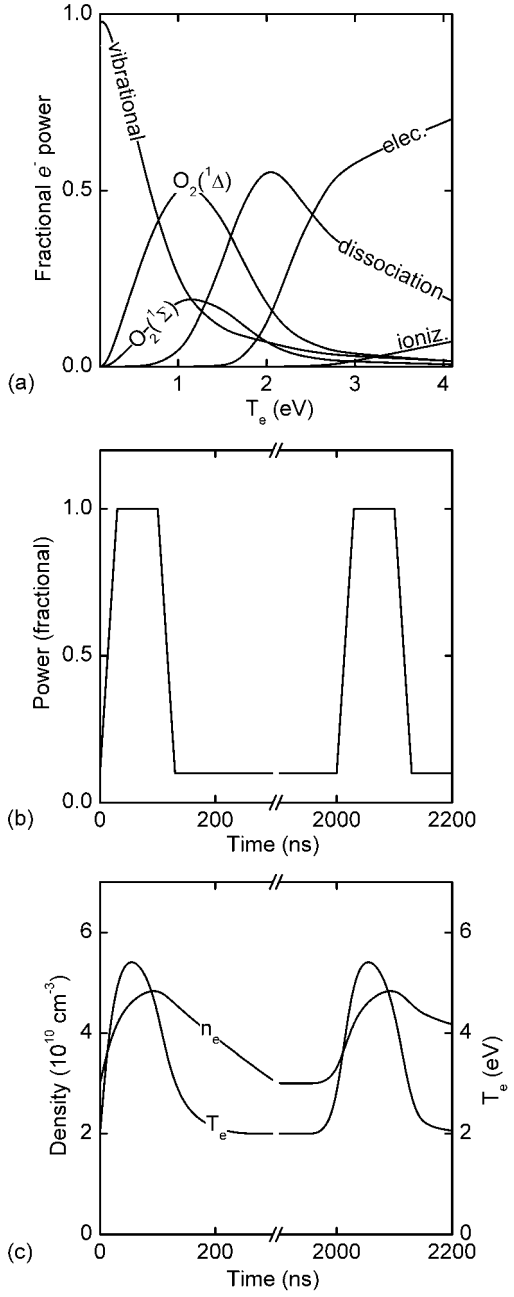

Fig. 5.7. Motivation for pulsed discharges. (a) Fraction of electron power deposited into various processes in pure O_2 as a function of T_e. (b) Waveform showing fraction of peak power deposited into the discharge for a pulse width of 100 ns and a pulse delay of 2 μs. (c) Approximate expected electron density and temperature in the quasi-steady discharge when using the pulsed scheme of (b). The pulsed scheme should reduce the average T_e in the discharge to ≈1 eV so that excitation to $O_2(^1\Delta)$ dominates the electron power deposition.

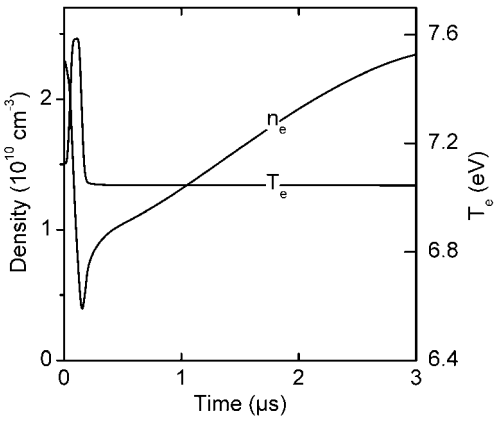

Fig. 5.8. Actual electron density and temperature at the midpoint of the quasi-steady discharge during a single pulse cycle. Pulse is 2.5 kW peak for 100 ns, with a pulse delay of 4 μs; average power is 340 W at 100 MHz. Other conditions are the same as for Fig. 5.1. The presence of a strongly attaching gas (O_2) causes the electron density to *decrease* during the pulse instead of increasing as shown in Fig. 5.6(c).

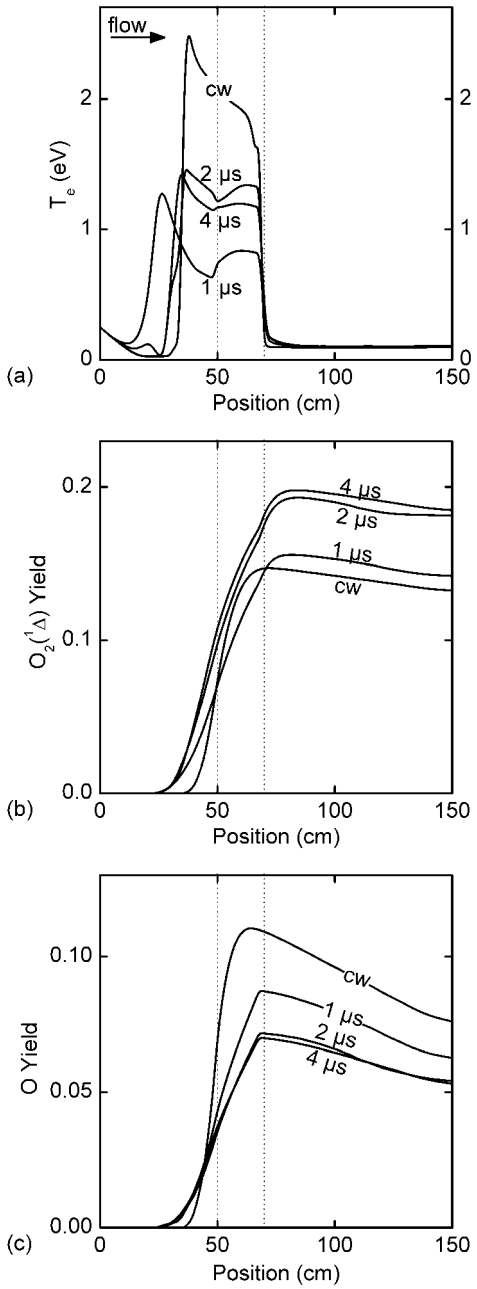

Fig. 5.9. Comparison of the results with 1, 2, and 4 μs delays between pulses for the quasi-steady discharge to the results for the continuous steady discharge. Average power is 340 W at 100 MHz; other conditions are the same as for Fig. 5.1. (a) Electron temperature when the background power is applied (the pulse is off). (b) $O_2(^1\Delta)$ yield and (c) O yield along the discharge. The electron temperature decreased from ≈2 eV to ≈1 eV for the pulsed cases – a value more favorable for $O_2(^1\Delta)$ production than for dissociation.

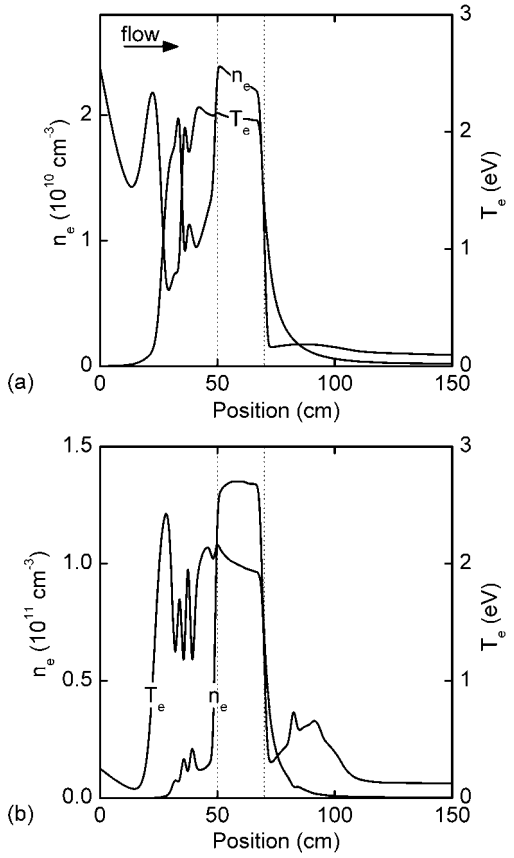

Fig. 5.10. Electron temperature and density instability observed in the quasi-steady simulation. Conditions were the same as for Fig. 5.1, except as noted below. (a) T_e and n_e when the wall capacitance is halved. (b) T_e and n_e when input power is > 1 kW. Decreasing the capacitance and increasing the power both cause the plasma zone to propagate significantly upstream, producing the instability.

5.11 References

1. Rakhimova, T.V., et al., *Radio-frequency plasma generation of singlet oxygen in O_2 and O_2:Ar(He) mixtures.* AIAA Paper 2003-4306, 2003.
2. Carroll, D.L., et al., *Recent Experimental Measurements of the ElectriCOIL System.* AIAA Paper 2003-4029, 2003.
3. Carroll, D.L., et al., *Measurement of positive gain on the 1315 nm transition of atomic iodine pumped by $O_2(a^1\Delta)$ produced in an electric discharge.* Applied Physics Letters, 2004. **85**(7): p. TBD.
4. Verdeyen, J.T., et al. *Diagnostic development for the ElectriCOIL flow system*. in *Proceedings of the Gas and Chemical Lasers and Intense Beam Applications III Conference*. 2002. San Jose, CA, 22-24 January 2002: SPIE, Bellingham, WA.
5. Carroll, D.L., et al., *Path to the measurement of positive gain on the 1315 nm transition of atomic iodine pumped by $O_2(a^1\Delta)$ produced in an electric discharge.* submitted to J. Quant. Elec., 2004.
6. Ionin, A.A., et al., *Non-self-sustained electric discharge in oxygen gas mixtures: singlet delta oxygen production.* Journal of Physics D: Applied Physics, 2003. **36**(8): p. 982-989.
7. Hill, A. *The next generation of controlled avalanche discharge gas lasers*. in *International Conference on Lasers*. 2000. Albuquerque, NM: STS Press.
8. Hicks, A., et al. *Singlet Oxygen Generation in a High Pressure Non-Self-Sustained Electric Discharge*. in *Gaseous Electronics Conference*. 2004. Bunratty, Ireland: APS.

6. CONCLUDING REMARKS

Zero- and one-dimensional (axially dependent) numerical models were developed for axially flowing discharges at moderate pressures. We applied these models to the problem of simulating He and O_2 discharges used to pump chemical oxygen-iodine lasers (COIL). The models facilitate investigation of plasma kinetics and flow induced effects on $O_2(^1\Delta)$ yields. The objective of this work was to provide insight into methods that could be used to optimize $O_2(^1\Delta)$ yield, ultimately leading to a functional electric discharge pumped COIL.

To first order, the zero-dimensional model showed that $O_2(^1\Delta)$ yield from He/O_2 discharges at moderate pressures was a function of the specific energy deposited into the O_2 species in the discharge, with peak yields occurring near 5 – 8 eV per molecule of inlet O_2. Variations in flow velocity, pressure, power, and mixture caused smaller second order effects. However, when the $O_2(^1\Sigma)$ density is included in the $O_2(^1\Delta)$ yield determination, the second order effects are considerably reduced, and yield is almost completely dependent on specific energy deposition.

The one-dimensional model confirmed the scaling result of the zero-dimensional model and also provided insight into the effects of axial transport, most notably, the expansion of the plasma zone upstream and downstream of the electrodes. As with the zero-dimensional model, the addition of He as a diluent was found to have a relatively small effect. Capacitive, inductive, and pulsed capacitive discharges were investigated. The pulsed discharges were shown to provide significantly increased $O_2(^1\Delta)$ yield and decreased dissociation relative to continuous discharges at the same specific energy

deposition. The pulsed discharges were the only schemes investigated in this study that showed significant deviation from the specific energy deposition scaling of $O_2(^1\Delta)$ yield.

The primary uncertainties in the models center on physical phenomena that were excluded – mostly 2-D and power supply feedback effects. No attempt was made to capture 2-D transport effects that can cause discharge instabilities and reduced $O_2(^1\Delta)$ yields. Neither was any attempt made to provide a feedback mechanism for the power deposition models. Rather, these simulations focused on the gas phase plasma kinetics and effects of axial transport of mass, momentum, and energy. As such, the well-developed kinetic and 1-D gas dynamic framework has been shown to have relatively small uncertainties. Further work should focus on accounting for the physical phenomena mentioned above. In particular, the inclusion of radial geometry would facilitate investigation of several types of discharge instabilities relevant to the study of electronegative gases. In addition, a true external circuit model would provide a means to obtain more accurate time-dependent results when a pulsed discharge is desired.

APPENDIX A. LIST OF REACTIONS FOR He/O_2 PLASMAS

A.1 Gas Phase Reaction Mechanism

Reaction	Rate constant [a, b]	Reference
$e + He \rightarrow He^* + e$	$f(T_e)$	[1]
$e + He \rightarrow He^* + e$	$f(T_e)$	[1]
$e + He \rightarrow He^+ + e + e$	$f(T_e)$	[2]
$e + He^* \rightarrow He^+ + e + e$	$f(T_e)$	[3]
$e + He^* \rightarrow He + e$	$f(T_e)$	c
$e + He^+ \rightarrow He^*$	$6.76\times10^{-13}T_e^{-0.5}$	[4]
$e + e + He^+ \rightarrow He^* + e$	$5.12\times10^{-27}T_e^{-4.5}$	[4]
$e + O_2 \rightarrow O^- + O$	$f(T_e)$	[5]
$e + O_2 \rightarrow O_2(v) + e$	$f(T_e)$	[5]
$e + O_2 \rightarrow O_2(v) + e$	$f(T_e)$	[5]
$e + O_2 \rightarrow O_2(v) + e$	$f(T_e)$	[5]
$e + O_2 \rightarrow O_2(v) + e$	$f(T_e)$	[5]
$e + O_2 \rightarrow O_2(^1\Delta) + e$	$f(T_e)$	[5]
$e + O_2 \rightarrow O_2(^1\Sigma) + e$	$f(T_e)$	[5]
$e + O_2 \rightarrow O + O + e$	$f(T_e)$	[5]
$e + O_2 \rightarrow O(^1D) + O + e$	$f(T_e)$	[5]
$e + O_2 \rightarrow O_2^+ + e + e$	$f(T_e)$	[5]
$e + O_2 \rightarrow O^+ + O + e + e$	$f(T_e)$	[6]
$e + O_2 + M \rightarrow O_2^- + M$	$3.60\times10^{-31}T_e^{-0.5}$	[7]
$e + O_2^+ \rightarrow O + O$	$1.20\times10^{-8}T_e^{-0.7}$	[8]
$e + O_2^+ \rightarrow O(^1D) + O$	$8.88\times10^{-9}T_e^{-0.7}$	[8]
$e + O_2(v) \rightarrow O^- + O$	$f(T_e)$	d
$e + O_2(v) \rightarrow O_2 + e$	$f(T_e)$	c
$e + O_2(v) \rightarrow O_2(^1\Delta) + e$	$f(T_e)$	e
$e + O_2(v) \rightarrow O_2(^1\Sigma) + e$	$f(T_e)$	e
$e + O_2(v) \rightarrow O + O + e$	$f(T_e)$	e
$e + O_2(v) \rightarrow O(^1D) + O + e$	$f(T_e)$	e
$e + O_2(v) \rightarrow O_2^+ + e + e$	$f(T_e)$	e
$e + O_2(v) \rightarrow O(^1D) + O(^1D) + e$	$f(T_e)$	e
$e + O_2(v) \rightarrow O^+ + O + e + e$	$f(T_e)$	e
$e + O_2(^1\Delta) \rightarrow O^- + O$	$f(T_e)$	[9]
$e + O_2(^1\Delta) \rightarrow O_2(^1\Sigma) + e$	$f(T_e)$	[10]

$e + O_2(^1\Delta) \rightarrow O_2 + e$	$f(T_e)$	c
$e + O_2(^1\Delta) \rightarrow O + O + e$	$f(T_e)$	e
$e + O_2(^1\Delta) \rightarrow O(^1D) + O + e$	$f(T_e)$	e
$e + O_2(^1\Delta) \rightarrow O_2^+ + e + e$	$f(T_e)$	e
$e + O_2(^1\Delta) \rightarrow O(^1D) + O(^1D) + e$	$f(T_e)$	e
$e + O_2(^1\Delta) \rightarrow O^+ + O + e + e$	$f(T_e)$	e
$e + O_2(^1\Sigma) \rightarrow O^- + O$	$f(T_e)$	f
$e + O_2(^1\Sigma) \rightarrow O_2(^1\Delta) + e$	$f(T_e)$	g
$e + O_2(^1\Sigma) \rightarrow O_2 + e$	$f(T_e)$	c
$e + O_2(^1\Sigma) \rightarrow O + O + e$	$f(T_e)$	e
$e + O_2(^1\Sigma) \rightarrow O(^1D) + O + e$	$f(T_e)$	e
$e + O_2(^1\Sigma) \rightarrow O_2^+ + e + e$	$f(T_e)$	e
$e + O_2(^1\Sigma) \rightarrow O(^1D) + O(^1D) + e$	$f(T_e)$	e
$e + O_2(^1\Sigma) \rightarrow O^+ + O + e + e$	$f(T_e)$	e
$e + O_3 \rightarrow O^- + O_2$	$f(T_e)$	[11]
$e + O_3 \rightarrow O_2^- + O$	$f(T_e)$	[11]
$e + O \rightarrow O(^1D) + e$	$f(T_e)$	[12]
$e + O \rightarrow O(^1S) + e$	$f(T_e)$	[12]
$e + O \rightarrow O^+ + e + e$	$f(T_e)$	[12]
$e + O(^1D) \rightarrow O + e$	$f(T_e)$	c
$e + O(^1D) \rightarrow O^+ + e + e$	$f(T_e)$	h
$e + O(^1S) \rightarrow O + e$	$f(T_e)$	c
$e + O(^1S) \rightarrow O^+ + e + e$	$6.60\times10^{-9} T_e^{\,0.6} \exp\left(-\frac{9.43}{T_e}\right)$	i
$e + O^- \rightarrow O + e + e$	$1.95\times10^{-12} T_e^{\,0.5} \exp\left(-\frac{3.4}{T_e}\right)$	[13]
$e + O^+ \rightarrow O(^1D)$	$5.30\times10^{-13} T_e^{\,-0.5}$	[4]
$e + e + O^+ \rightarrow O(^1D) + e$	$5.12\times10^{-27} T_e^{\,-4.5}$	[4]
$O^- + O_2^+ \rightarrow O + O_2$	$2\times10^{-7} T_0^{\,-1}$	[8]
$O^- + O_2^+ \rightarrow O + O + O$	1×10^{-7}	[8]
$O^- + O^+ \rightarrow O + O$	$2\times10^{-7} T_0^{\,-1}$	[8]
$O^- + He^+ \rightarrow O + He$	$2\times10^{-7} T_0^{\,-1}$	[8]
$O_2^- + O_2^+ \rightarrow O_2 + O_2$	$2\times10^{-7} T_0^{\,-1}$	[8]
$O_2^- + O_2^+ \rightarrow O_2 + O + O$	1×10^{-7}	[8]
$O_2^- + O^+ \rightarrow O_2 + O$	$2\times10^{-7} T_0^{\,-1}$	[8]
$O_2^- + He^+ \rightarrow O_2 + He$	$2\times10^{-7} T_0^{\,-1}$	[8]
$O_3^- + O_2^+ \rightarrow O_3 + O_2$	$2\times10^{-7} T_0^{\,-1}$	[8]

$O_3^- + O_2^+ \rightarrow O_3 + O + O$	1×10^{-7}	[8]
$O_3^- + O^+ \rightarrow O_3 + O$	$2\times10^{-7}T_0^{-1}$	[8]
$O_3^- + He^+ \rightarrow O_3 + He$	$2\times10^{-7}T_0^{-1}$	[8]
$O^- + O_2^+ + M \rightarrow O + O_2 + M$	$2\times10^{-25}T_0^{-2.5}$ $cm^6 s^{-1}$	[8]
$O^- + O^+ + M \rightarrow O + O + M$	$2\times10^{-25}T_0^{-2.5}$ $cm^6 s^{-1}$	[8]
$O^- + He^+ + M \rightarrow O + He + M$	$2\times10^{-25}T_0^{-2.5}$ $cm^6 s^{-1}$	[8]
$O^- + O \rightarrow O_2 + e$	$2\times10^{-10}T_0^{0.5}$	[14]
$O^- + O_2(^1\Delta) \rightarrow O_3 + e$	$3\times10^{-10}T_0^{0.5}$	[14]
$O^- + O_2(^1\Sigma) \rightarrow O + O_2 + e$	$6.9\times10^{-10}T_0^{0.5}$	[8]
$O^- + O_2 \rightarrow O_3 + e$	$5\times10^{-15}T_0^{0.5}$	[8]
$O^- + O_3 \rightarrow O_2 + O_2 + e$	$3.01\times10^{-10}T_0^{0.5}$	[14]
$O^- + O_3 \rightarrow O_3^- + O$	$1.99\times10^{-10}T_0^{0.5}$	[14]
$O^- + O_3 \rightarrow O_2^- + O_2$	$1.02\times10^{-11}T_0^{0.5}$	[14]
$O_2^- + O \rightarrow O^- + O_2$	$1.5\times10^{-10}T_0^{0.5}$	[14]
$O_2^- + O \rightarrow O_3 + e$	$1.5\times10^{-10}T_0^{0.5}$	[14]
$O_2^- + O_2(^1\Delta) \rightarrow e + O_2 + O_2$	$2\times10^{-10}T_0^{0.5}$	[14]
$O_2^- + O_3 \rightarrow O_3^- + O_2$	$6\times10^{-10}T_0^{0.5}$	[14]
$O_3^- + O \rightarrow O_2^- + O_2$	$2.5\times10^{-10}T_0^{0.5}$	[14]
$O + O^+ \rightarrow O + O^+$	$1\times10^{-9}T_0^{0.5}$	j
$O + O^+ + M \rightarrow O_2^+ + M$	$1\times10^{-29}T_0^{0.5}$ $cm^6 s^{-1}$	[8]
$O_2 + O_2^+ \rightarrow O_2 + O_2^+$	$1\times10^{-9}T_0^{0.5}$	[15]
$O^+ + O_2 \rightarrow O_2^+ + O$	$2\times10^{-11}T_0^{-0.4}$	[14]
$O^+ + O_3 \rightarrow O_2^+ + O_2$	1×10^{-10}	[8]
$O(^1D) + O \rightarrow O + O$	8×10^{-12}	[8]
$O(^1D) + O_2 \rightarrow O + O_2(^1\Sigma)$	$2.56\times10^{-11}\exp\left(\frac{67}{T_g}\right)$	[16]
$O(^1D) + O_2 \rightarrow O + O_2(^1\Delta)$	$1.6\times10^{-12}\exp\left(\frac{67}{T_g}\right)$	[16]
$O(^1D) + O_2 \rightarrow O + O_2$	$4.8\times10^{-12}\exp\left(\frac{67}{T_g}\right)$	[16]
$O(^1D) + O_3 \rightarrow O_2 + O + O$	1.2×10^{-10}	[17]
$O(^1D) + O_3 \rightarrow O_2 + O_2$	1.2×10^{-10}	[18]

$O(^1D) + He \rightarrow O + He$	1×10^{-13}	[19]
$O(^1S) + O_2 \rightarrow O(^1D) + O_2$	$3.2\times10^{-12}\exp\left(-\frac{850}{T_g}\right)$	[18]
$O(^1S) + O_2 \rightarrow O + O_2$	$1.6\times10^{-12}\exp\left(-\frac{850}{T_g}\right)$	[18]
$O(^1S) + O_2(^1\Delta) \rightarrow O + O_2$	1.1×10^{-10}	[8], k
$O(^1S) + O_2(^1\Delta) \rightarrow O(^1D) + O_2(^1\Sigma)$	2.9×10^{-11}	[8]
$O(^1S) + O_2(^1\Delta) \rightarrow O + O + O$	3.2×10^{-11}	[8]
$O(^1S) + O \rightarrow O(^1D) + O$	$1.67\times10^{-11}\exp\left(-\frac{300}{T_g}\right)$	[18]
$O(^1S) + O \rightarrow O + O$	$3.33\times10^{-11}\exp\left(-\frac{300}{T_g}\right)$	[18]
$O(^1S) + O_3 \rightarrow O_2 + O_2$	5.8×10^{-10}	[18], l
$O_2(^1\Delta) + O \rightarrow O_2 + O$	2×10^{-16}	[18]
$O_2(^1\Delta) + O_2 \rightarrow O_2 + O_2$	$3\times10^{-18}\exp\left(-\frac{200}{T_g}\right)$	[16]
$O_2(^1\Delta) + O_2(^1\Delta) \rightarrow O_2 + O_2$	$9\times10^{-17}\exp\left(-\frac{560}{T_g}\right)$	[18], m
$O_2(^1\Delta) + O_2(^1\Delta) \rightarrow O_2(^1\Sigma) + O_2$	$9\times10^{-17}\exp\left(-\frac{560}{T_g}\right)$	m
$O_2(^1\Delta) + O_2 \rightarrow O + O_3$	$2.95\times10^{-21}T_0^{0.5}$	
$O_2(^1\Delta) + O_3 \rightarrow O_2 + O_2 + O$	$5.2\times10^{-11}\exp\left(-\frac{2840}{T_g}\right)$	[17]
$O_2(^1\Delta) + He \rightarrow O_2 + He$	$8\times10^{-21}T_0^{0.5}$	[20]
$O_2(^1\Sigma) + O_2(^1\Sigma) \rightarrow O_2(^1\Delta) + O_2$	$3.6\times10^{-17}T_0^{0.5}$	[16], j
$O_2(^1\Sigma) + O_2 \rightarrow O_2(^1\Delta) + O_2$	$3.6\times10^{-17}T_0^{0.5}$	[16]
$O_2(^1\Sigma) + O_2 \rightarrow O_2 + O_2$	$4\times10^{-18}T_0^{0.5}$	[16]
$O_2(^1\Sigma) + O \rightarrow O_2(^1\Delta) + O$	$7.2\times10^{-14}T_0^{0.5}$	[16]
$O_2(^1\Sigma) + O \rightarrow O_2 + O$	$8\times10^{-15}T_0^{0.5}$	[16]
$O_2(^1\Sigma) + O_3 \rightarrow O + O_2 + O_2$	$7.33\times10^{-12}T_0^{0.5}$	[21]
$O_2(^1\Sigma) + O_3 \rightarrow O_2(^1\Delta) + O_3$	$7.33\times10^{-12}T_0^{0.5}$	[21]
$O_2(^1\Sigma) + O_3 \rightarrow O_2 + O_3$	$7.33\times10^{-12}T_0^{0.5}$	[21]

$O_2(^1\Sigma) + He \rightarrow O_2(^1\Delta) + He$	$1\times10^{-17} T_0^{0.5}$	j
$O_2(v) + O \rightarrow O_2 + O$	$1\times10^{-14} T_0^{0.5}$	[16], j
$O_2(v) + O_2 \rightarrow O_2 + O_2$	$1\times10^{-14} T_0^{0.5}$	[16], j
$O_2(v) + He \rightarrow O_2 + He$	$1\times10^{-14} T_0^{0.5}$	[16], j
$O + O + O_2 \rightarrow O_2 + O_2$	$2.56\times10^{-34} T_0^{-0.63}$ $cm^6 s^{-1}$	[8]
$O + O + O \rightarrow O_2 + O$	$9.21\times10^{-34} T_0^{-0.63}$ $cm^6 s^{-1}$	[8]
$O + O + He \rightarrow O_2 + He$	1×10^{-33} $cm^6 s^{-1}$	[8, 20]
$O + O + O_2 \rightarrow O_2(^1\Delta) + O_2$	$1.93\times10^{-35} T_0^{-0.63}$ $cm^6 s^{-1}$	[8]
$O + O + O \rightarrow O_2(^1\Delta) + O$	$6.93\times10^{-35} T_0^{-0.63}$ $cm^6 s^{-1}$	[8]
$O + O + He \rightarrow O_2(^1\Delta) + He$	9.88×10^{-35} $cm^6 s^{-1}$	[8, 20]
$O + O_2 + O_2 \rightarrow O_3 + O_2$	$6\times10^{-34} T_0^{-2.8}$ $cm^6 s^{-1}$	[16]
$O + O_2 + He \rightarrow O_3 + He$	$3.4\times10^{-34} T_0^{-1.2}$ $cm^6 s^{-1}$	[20]
$O + O_2 + O \rightarrow O_3 + O$	$3.4\times10^{-34} T_0^{-1.2}$ $cm^6 s^{-1}$	j
$O + O_3 \rightarrow O_2 + O_2$	$8\times10^{-12} \exp\left(-\frac{2060}{T_g}\right)$	[16]
$O_3 + M \rightarrow O_2 + O + M$	$1.56\times10^{-9} \exp\left(-\frac{11{,}490}{T_g}\right)$	[22], j
$He^* + He^* \rightarrow He + He^+ + e$	$1.5\times10^{-9} T_0^{0.5}$	[23]
$He^* + O_2 \rightarrow O_2^+ + He + e$	$2.54\times10^{-10} T_0^{0.5}$	[24]
$He^* + O_3 \rightarrow O_2^+ + O + He + e$	$2.54\times10^{-10} T_0^{0.5}$	[24], n
$He^* + O_2(^1\Sigma) \rightarrow O_2^+ + He + e$	$2.54\times10^{-10} T_0^{0.5}$	[24], n
$He^* + O \rightarrow O^+ + He + e$	$2.54\times10^{-10} T_0^{0.5}$	[24], n
$He^* + O(^1D) \rightarrow O^+ + He + e$	$2.54\times10^{-10} T_0^{0.5}$	[24], n
$He^* + O(^1S) \rightarrow O^+ + He + e$	$2.54\times10^{-10} T_0^{0.5}$	[24], n
$He^+ + O_2 \rightarrow O^+ + O + He$	$1.07\times10^{-9} T_0^{0.5}$	[14]
$He^+ + O_3 \rightarrow O^+ + O_2 + He$	$1.07\times10^{-9} T_0^{0.5}$	n
$He^+ + O_2 \rightarrow O_2^+ + He$	$3.3\times10^{-11} T_0^{0.5}$	[14]
$He^+ + O_2(^1\Delta) \rightarrow O^+ + O + He$	$1.07\times10^{-9} T_0^{0.5}$	n
$He^+ + O_2(^1\Delta) \rightarrow O_2^+ + He$	$3.3\times10^{-11} T_0^{0.5}$	n
$He^+ + O \rightarrow O^+ + He$	$5\times10^{-11} T_0^{0.5}$	j
$He^+ + O(^1D) \rightarrow O^+ + He$	$5\times10^{-11} T_0^{0.5}$	j

$He^+ + O(^1S) \rightarrow O^+ + He$	$5\times10^{-11}T_0^{0.5}$	j
$He + He^+ \rightarrow He + He^+$	$1\times10^{-9}T_0^{0.5}$	[15]

[a] Rate coefficients have units of $cm^3\ s^{-1}$ unless otherwise noted. $T_0 = \left(T_g/300\right)$; T_g has units K; T_e has units eV.

[b] Rate coefficient obtained from EED using cross-section from indicated reference. Rate coefficients are compiled as a function of E/N and interpolated based on instantaneous values of T_e.

[c] Superelastic cross-section calculated using detailed balance for excitation from lower state.

[d] Estimated to have the same cross-section as the ground state reaction.

[e] Cross-section estimated by shifting and scaling the ground state cross-section by the excitation threshold.

[f] Cross-section estimated by shifting and scaling the $O_2(^1\Delta)$ cross-section by the excitation threshold.

[g] Superelastic cross-section calculated using detailed balance for excitation from $O_2(^1\Delta)$.

[h] Cross-section estimated by shifted the ground state cross-section by the excitation threshold.

[i] Scaled from O ionization rate expression [13] using correlation given by Vriens [25].

[j] Estimated.

[k] Rate given by [8]; assumed branching to ground state.

[l] Rate given by [18] with branching given by [8].

[m] Rate given by [18]; assumed half branches to O_2 and half to $O_2(^1\Delta)$.

[n] Estimated same as O_2.

A.2 Wall Reaction Mechanism

Wall reaction	Reaction probability	Reference
$O_2(v) + wall \rightarrow O_2$	0.20	
$O_2(^1\Delta) + wall \rightarrow O_2$	10^{-5}	[8]
$O_2(^1\Sigma) + wall \rightarrow O_2$	0.02	[8]
$O + wall \rightarrow ½\ O_2$	0.02	[8]
$O(^1D) + wall \rightarrow O$	1.00	[8]
$O(^1S) + wall \rightarrow O$	1.00	[8]
$He(^2S) + wall \rightarrow He$	1.00	
$M^+ + wall \rightarrow M$	1.00	

A.3 References

1. Boeuf, J.P. and E. Marode, *A Monte Carlo analysis of an electron swarm in a nonuniform field: the cathode region of a glow discharge in helium.* Journal of Physics D: Applied Physics, 1982. **15**(11): p. 2169-2187.
2. Rapp, D. and P. Englander-Golden, *Total Cross Sections for Ionization and Attachment in Gases by Electron Impact: I. Positive Ionization.* Journal of Chemical Physics, 1965. **43**(5): p. 1464-1479.
3. Vriens, L., *Calculation of absolute ionisation cross sections of He, He^*, He^+, Ne, Ne^*, Ne^+, Ar, Ar^*, Hg and Hg*.* Physics Letters, 1964. **8**(4): p. 260-261.
4. Bekefi, G., *Chapter 4*, in *Radiation Processes in Plasmas*. 1966, Wiley: New York.
5. Phelps, A.V. *Tabulations of collision cross-sections and calculated transport and reaction coefficients for electron collisions with O_2.* in *JILA Information Center Report No. 28*. 1985. Boulder, Colorado: University of Colorado.
6. Krishnakumar, E. and S.K. Srivastava, *Cross-sections for electron impact ionization of O_2.* International Journal of Mass Spectrometry and Ion Processes, 1992. **113**(1): p. 1-12.
7. Itikawa, Y., et al., *Cross Sections for Collisions of Electrons and Photons with Oxygen Molecules.* Journal of Physical and Chemical Reference Data, 1989. **18**(1): p. 23-42.
8. Gordiets, B.F., et al., *Kinetic model of a low-pressure N_2-O_2 flowing glow discharge.* IEEE Transactions on Plasma Science, 1995. **23**(4): p. 750-768.
9. Burrow, P.D., *Dissociative attachment from the $O_2(^1\Delta_g)$ state.* Journal of Chemical Physics, 1973. **59**(9): p. 4922-4931.

10. Hall, R.I. and S. Trajmar, *Scattering of 4.5 eV electrons by ground ($x^3\Sigma_g^-$) state and metastable ($a^1\Delta_g$) oxygen molecules.* Journal of Physics B: Atomic and Molecular Physics, 1975. **8**(12): p. L293-L296.

11. Matejcik, S., et al., *Electron attachment to molecules and clusters of atmospheric relevance: oxygen and ozone.* Plasma Sources Science and Technology, 1997. **6**(2): p. 140-146.

12. Laher, R.R. and F.R. Gilmore, *Updated excitation and ionization cross sections for electron impact on atomic oxygen.* Journal of Physical and Chemical Reference Data, 1990. **19**: p. 277.

13. Meeks, E., et al., *Modeling of SiO_2 deposition in high density plasma reactors and comparisons of model predictions with experimental measurements.* Journal of Vacuum Science and Technology A, 1998. **16**(2): p. 544-563.

14. Ikezoe, Y., et al. *Gas Phase Ion-Molecule Reaction Rate Constants Through 1986*. in *Ion Reaction Research Group of the Mass Spectroscopy Society of Japan*. 1987. Tokyo, Japan.

15. Ellis, H.W., et al., *Transport properties of gaseous ions over a wide energy range. Part III.* Atomic Data and Nuclear Data Tables, 1984. **31**: p. 113-151.

16. Atkinson, R., et al., *Evaluated Kinetic and Photochemical Data for Atmospheric Chemistry: Supplement V.* Journal of Physical and Chemical Reference Data, 1997. **26**: p. 521-1011.

17. Atkinson, R., et al., *Evaluated Kinetic and Photochemical Data for Atmospheric Chemistry: Supplement VI (O_x, HO_x, NO_x, SO_x).* Journal of Physical and Chemical Reference Data, 1997. **26**: p. 1329-1499.

18. Herron, J.T. and D.S. Green, *Chemical Kinetics Database and Predictive Schemes for Nonthermal Humid Air Plasma Chemistry. Part II. Neutral Species Reactions.* Plasma Chemistry and Plasma Processing, 2001. **21**(3): p. 459-481.

19. Shi, J. and J.R. Barker, International Journal of Chemical Kinetics, 1990. **22**: p. 1283.

20. *NIST Standard Reference Database 17-2Q98*. 1998. National Institute of Standards and Technology, Gaithersburg, MD 20899.

21. Choo, K.W. and M.T. Leu, *Rate Constants for the Quenching of Metastable $O_2(^1\Sigma_g^+)$ Molecules.* International Journal of Chemical Kinetics, 1985. **17**: p. 1155.

22. Eliasson, B. and U. Kogelschatz. *Basic Data for Modelling of Electrical Discharges in Gases: Oxygen*. in *Brown Boveri Technical Report LKR 86-11 C*. 1986.

23. Deloche, R., et al., *High-pressure helium afterglow at room temperature.* Physical Review A, 1976. **13**(3): p. 1140-1176.

24. Pouvesle, J.M., et al., *Study of two-body and three-body channels for the reaction of metastable helium atoms with selected atomic and molecular species.* Journal of Chemical Physics, 1988. **88**(5): p. 3061-3071.

25. Vriens, L., *Binary-Encounter Electron-Atom Collision Theory*. Physical Review, 1966. **141**(1): p. 88-92.